

Overview of refractive index sensors comprising photonic crystal fibers based on the surface plasmon resonance effect [Invited]

Chao Liu (刘超)¹, Jingwei Lü (吕靖薇)¹, Wei Liu (刘伟)¹, Famei Wang (汪发美)¹, and Paul K. Chu (朱剑豪)²

¹School of Physics and Electronic Engineering, Northeast Petroleum University, Daqing 163318, China

²Department of Physics, Department of Materials Science & Engineering, and Department of Biomedical Engineering, City University of Hong Kong, Hong Kong, China

*Corresponding author: msm-liu@126.com

Received January 21, 2021 | Accepted March 17, 2021 | Posted Online August 26, 2021

Optical fibers have been widely applied to telecommunication, imaging, lasers, and sensing. Among the different types of fibers, photonic crystal fibers (PCFs), also called microstructured optical fibers, characterized by air holes arranged along the length of fibers have experienced tremendous advance due to their unique advantages. They are regarded as a desirable platform to excite surface plasmon resonance (SPR) because of easy realization of phase matching conditions between the fundamental core mode and the plasmonic mode, which plays a critical role in miniaturization and integration of SPR sensors. In this mini-review, the current status of PCF sensors based on SPR is summarized. The theory of SPR is discussed, and simulation methods for PCF-SPR sensors are described. The important parameters including the refractive index detection range, resonance wavelength, and spectral sensitivity responsible for the sensing properties of PCF-SPR sensors are reviewed. The fabrication and the comparison of performances are also illustrated, and, finally, the challenges and future perspectives are outlined.

Keywords: photonic crystal fibers; surface plasmon resonance; refractive index; sensors.

DOI: [10.3788/COL202119.102202](https://doi.org/10.3788/COL202119.102202)

1. Introduction

Surface plasmon resonance (SPR) is a critical physical-optical phenomenon involving excitation of electron density oscillations at metal-dielectric interfaces under the irradiation of *p*-polarized light waves^[1–4]. As a versatile sensing technique, SPR has the outstanding advantage of extremely high sensitivity to variations of the refractive index (RI) of analytes, thereby greatly applied to biomedicine, biology, and chemistry monitoring^[5–8]. The first, to the best of our knowledge, documented observation of surface plasmons was reported in 1902 when Wood observed narrow dark bands in the diffraction spectrum of metallic gratings illuminated with polychromatic light^[9]. SPR excited by total internal reflection was observed by Otto^[10] as well as Kretschmann and Raether^[11], and the great potential of SPR sensing technology pertaining to detection of chemical and biological substances has spurred growing interest^[12–16]. The conventional operating platform to excite SPR is based on the total internal reflection prism of the Kretschmann and Otto configuration. However, the Kretschmann–Raether prism configuration suffers from drawbacks such as bulky mechanical

equipment, large size, and non-remote measurements, and thus new sensing platforms with miniaturization and remote sensing capabilities are highly desirable^[17,18].

Driven by the large demand for miniaturization and integration and because optical fibers can transmit light waves based on total internal reflection, optical fibers constitute a desirable platform to excite SPR when plasmonic materials are coated on the surface of the fiber core^[19,20]. Optical fiber sensors based on SPR offer a number of advantages over traditional electronic sensors, for example, high sensitivity, small size, immunity to electromagnetic interference, remote detection, and resistance against corrosive media^[21–27]. These prominent features bode well for electromagnetic wave transmission in silica optical fibers, and, as a result of the great efforts and developments in the past decades, the impact of optical fiber sensor technology is becoming evident.

The recent development of optical fiber sensors coincides with the rapid advance of micro/nano-fabrication technology giving rise to novel photonic crystal fibers (PCFs)^[28–31]. A PCF is essentially a microstructured optical fiber consisting of a silica core surrounded by a periodic lattice of air holes along

the length of the fiber^[29]. The PCF has become a promising platform for SPR because of unique features that are difficult for conventional single-mode fibers (SMFs), for instance, single-mode operation over an extended range of operating wavelengths^[32], large mode area^[33], soliton propagation and continuum generation^[34,35], as well as overall controllable dispersion^[36]. Furthermore, PCFs are attractive to SPR sensing due to the flexible air hole arrangements; thereby, the RIs of the core and cladding can be scientifically tuned. The working principle of PCF-SPR sensors is to fulfill the phase matching condition, i.e., the coupling of the core-guided mode and the surface plasmon polaritons (SPPs) mode^[37]. In the past decade, PCF-SPR sensors have become a hot research area in the optical sensing field, and various types of PCF-SPR sensors have been proposed and investigated theoretically to cater to a myriad of applications^[38–43]. Based on the physical mechanisms that govern enhanced coupling between the core-guided mode and the plasmonic mode, most of the research efforts have focused on the following aspects: (1) broadening the RI detection range, (2) adjusting the resonance wavelength, and (3) increasing the sensing sensitivity.

Owing to the large impact of the technology, many papers have been published on PCF-SPR sensors, and our current knowledge is that the proper design and optimization determine the sensing properties of PCF-SPR sensors, for example, in bio-sensing and temperature and concentration measurements. In addition to Zhao *et al.*, who summarized the progress of PCF-SPR sensors in 2017 and completed an overview of chemical sensors^[44], there have been other reviews on PCF-SPR sensors with the localized SPR (LSPR) structures^[45–48]. The PCF-SPR sensors described in these articles are classified by the microstructure of the sensors. Herein, the current status of PCF-SPR RI sensors is reviewed. The physical principles governing SPRs are discussed, and the important simulation methods for PCF-SPR sensors are summarized. This review addresses the desirable attributes of PCF-SPR sensors including wide RI detection ranges, controllable resonance wavelengths, and high sensitivity. Different PCF-SPR sensors with unique structures and their sensing characteristics are also discussed.

2. Physical Principle of SPR

SPR is a phenomenon about optical excitation of surface plasmon waves (SPWs) by the method of attenuated total reflection except electron excitation. Before discussing PCF-SPR sensors, the SPR theory is described. The prism-structure model proposed by Otto^[10] and Kretschmann *et al.*^[11] forms the basis of PCF-SPR sensors, as shown in Fig. 1. There are two physical concepts in SPR excitation, namely, the SPW and evanescent wave.

2.1. Surface plasmon wave

The SPW is a charge-density oscillation that exists at the interface between a metal thin film and a dielectric substrate with

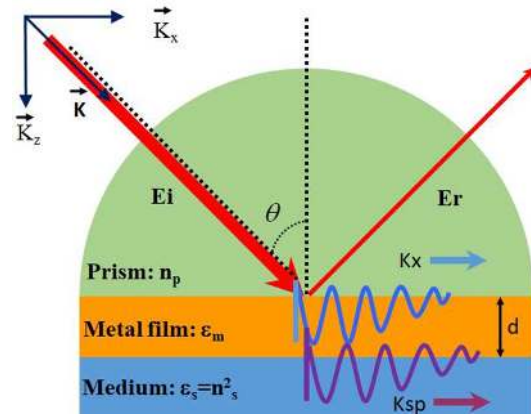


Fig. 1. SPR excitation by prism coupling using the Kretschmann configuration.

dielectric constants of opposite signs. The wave vector of SPW reaches the maximum value at the interface and decays evanescently into both media. The magnetic vector of the SPW is perpendicular to the propagation direction of the SPW and parallel to the plane of interface, the so-called TM-polarized wave. The propagation constant (k_{sp}) of SPW propagating at the interface between the dielectric and metal film can be defined as^[49]

$$k_{sp} = \frac{\omega}{c} \sqrt{\frac{\epsilon_m \epsilon_s}{\epsilon_m + \epsilon_s}} = \frac{\omega}{c} \sqrt{\frac{\epsilon_m n_s^2}{\epsilon_m + n_s^2}}, \quad (1)$$

where ϵ_m and n_s are the dielectric constant of the metal ($\epsilon_m = \epsilon_{mr} + i\epsilon_{mi}$) and RI of the dielectric materials, respectively. As indicated by Eq. (1), SPW is supported by the structure provided that $\epsilon_{mr} < -n_s^2$. At optical wavelengths, this condition is fulfilled with the aid of materials such as Au, Ag, Al, graphene, MoS₂, TiO₂, and In₂O₅Sn (ITO)^[44,50,51]. Among these plasmonic materials, Au and Ag are the most common. Equation (1) shows that the propagation constant (k_{sp}) of SPW is sensitive to the RI of the surrounding medium, and this phenomenon can be exploited in sensing. However, it is difficult and also inconvenient to measure and monitor the k_{sp} value of SPW using the current apparatus, and a more effective and maneuverable approach to excite SPW is required.

2.2. SPR excitation by the evanescent wave

The evanescent wave is central to SPR sensing, and it is conveniently considered based on the total internal reflection. Supposing an electromagnetic plane wave propagates in a surrounding medium, which is expressed mathematically by electric field E ,

$$E = E_0 \exp j(\omega t - \mathbf{k} \cdot \mathbf{r}) = E_0 \exp j(\omega t - k_x x - k_y y - k_z z), \quad (2)$$

where E_0 denotes the amplitude, ω is the angular frequency, \mathbf{k} is the wave vector, $\mathbf{r} = (x, y, z)$ is the position vector, and $j = \sqrt{-1}$.

The direction of the wave vector k is parallel to that of the wave propagation, and its magnitude is given by

$$k = \sqrt{k_x^2 + k_y^2 + k_z^2} = n \frac{2\pi}{\lambda} = n \frac{\omega}{c}, \quad (3)$$

where λ and c are the wavelength and velocity in vacuum, respectively. In the Kretschmann configuration shown in Fig. 1, there is only one traveling wave parallel to the interface:

$$E_{ev} = E_0 e^{-k_y y} \exp j(\omega t - k_x x). \quad (4)$$

The amplitude of the electric field (E_{ev}) decays exponentially along the vertical direction. The electric field propagates in the direction along the metal surface, and it is called the evanescent wave. The propagation constant of the evanescent wave k_{ev} is given by the following expression:

$$k_{ev} = k_x = \frac{\omega}{c} \sqrt{\epsilon_0} \sin \theta, \quad (5)$$

where θ is the incident angle, and ϵ_0 refers to the dielectric constant of the prism. The penetration depth is on the order of half a wavelength. This explains the interface sensitivity of the evanescent field because an electromagnetic field is only present close to the interface. Therefore, slight variations of dielectric property in the vicinity of the interface can affect this field.

SPW is not excited by an arbitrary light beam, and the phase matching conditions must be satisfied. It is a TM-polarized wave, so only TM polarized waves may excite SPW. The dispersion relation of SPW exhibits a nonlinear characteristic, and the momentum of the SPW is larger than that of light in free space for the same frequency, resulting in momentum mismatch between the light and SPW. The mismatch may be overcome by the evanescent wave from the prism coupler. In the prism configuration, the dispersion relation for the light wave and metal shows an intersection and therefore, SPW may be excited by the coupling light wave, as shown in Fig. 2.

In the three-layer system 0/1/2: prism/metal/medium geometry, as shown in Fig. 1, the reflected intensity is determined by Fresnel equations and the reflectivity R for p -polarized light,

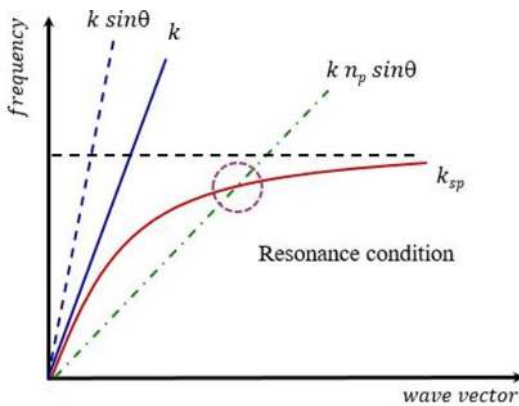


Fig. 2. Dispersion relation of TM incident light coupling with SPP.

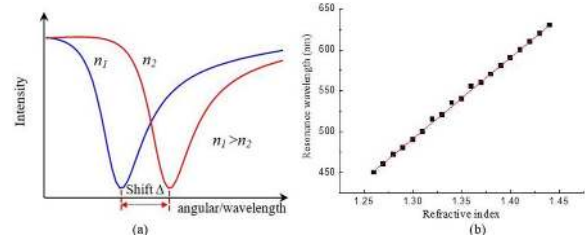


Fig. 3. Methodology of SPR measurement: (a) SPR spectra for different RIs and (b) relationship between the wavelength and RI.

with E_i^p the incident and E_r^p the reflected field, is given by Eq. (6)^[49]:

$$R = |r_{012}^p|^2 = \left| \frac{E_r^p}{E_i^p} \right|^2 = \left| \frac{r_{01}^p + r_{12}^p \exp(2ik_{z1}d)}{1 + r_{01}^p r_{12}^p \exp(2ik_{z1}d)} \right|^2, \quad (6)$$

where d is the thickness of the metal layer, and r_{ik}^p is the reflection coefficient at the interfaces of the three-layer system defined by

$$r_{ik}^p = \left(\frac{k_{zi}}{\epsilon_i} - \frac{k_{zk}}{\epsilon_k} \right) / \left(\frac{k_{zi}}{\epsilon_i} + \frac{k_{zk}}{\epsilon_k} \right), \quad (7)$$

$$k_{z1} = \sqrt{k_0^2 \epsilon_k - k_x^2}, \quad (8)$$

where k_{z1} is the z component of the wave vector in the metal film.

When the phase matching point between the plasmon wave and evanescent wave is satisfied according to Eq. (9), a dip occurs in the reflectivity curve, as shown in Fig. 3. The relationship between the resonance wavelength/angle and RI of the analyte can be described, for example, as shown in Fig. 3(b), to enable SPR sensing of the analyte. From the perspective of practical applications, a linear relationship between them is preferred:

$$k_{ev} = \frac{\omega}{c} \sqrt{\epsilon_0} \sin \alpha = k_{sp} = \text{Re} \left(\frac{\omega}{c} \sqrt{\frac{\epsilon_m \epsilon_s}{\epsilon_m + \epsilon_s}} \right). \quad (9)$$

3. Simulation, Characteristics, and Fabrication of PCF-SPR Sensors

3.1. Simulation method for PCF-SPR sensors

Theoretical simulation is an effective and powerful tool to evaluate the sensing performance of sensors before actual fabrication. Since PCF-SPR sensors are complicated owing to the large number of design parameters and degree of energy coupling between the fundamental core mode and plasmonic mode, it is crucial to understand the detailed influence of the structural parameters of the PCF and plasmonic materials on the optical properties of the sensors in order to accurately predict the sensing characteristics.

The design of a typical PCF-SPR sensor involves at least a dozen parameters such as the air hole size, plasmonic-layer thickness, and fiber core diameter. PCF-SPR simulation includes the process of selecting the optimal design and using models to predict the sensing performance for each structural combination. The primary advantage of combining computer simulation and modal analysis is that the modeler can try different approaches to obtain the solution for the same problem in order to design and optimize structural parameters of the desired PCF-SPR sensors.

According to the physics of SPR, when the phase matching conditions in PCF-SPR sensors are achieved, the largest energy is transferred from the fundamental core-guided mode to the plasmonic mode, leading to loss of the transmitted energy in fibers. Mathematically, the confinement loss α_{loss} is often employed to describe the sensing properties of PCF-SPR sensors, which is expressed as^[52]

$$\alpha_{\text{loss}} = 8.686 \times \frac{2\pi}{\lambda} \text{Im}(n_{\text{eff}}) \times 10^7 \text{ (dB/cm)}, \quad (10)$$

where λ denotes the incident wavelength in vacuum with a unit of nanometer, and $\text{Im}(n_{\text{eff}})$ is the imaginary part of the effective RI of the core-guided mode. When the dependence of $\text{Re}(n_{\text{eff}})$ of SPW and the fundamental core-guided mode on wavelength λ is plotted, phase matching conditions are fulfilled when the resonant wavelength coincides with the intersection between the dispersion relations of the fundamental core-guided mode and plasmonic mode. In addition, with regard to common plasmonic materials (Au, Ag), the dielectric function relations can be obtained from the Drude models. For example, the relative permittivity of Ag (ϵ_{Ag}) is obtained by the extended Drude model for wavelengths from 180 nm to 2000 nm^[53,54]:

$$\epsilon_{\text{Ag}}(\omega) = \epsilon_{\infty} + \frac{\sigma/\epsilon_0}{i\omega} + \sum_{p=1}^4 \frac{C_p}{\omega^2 + A_p i\omega + B_p}. \quad (11)$$

In order to assess the sensing performance of PCF-SPR sensors, there are three important parameters: spectral sensitivity, amplitude sensitivity, and RI resolution. The spectral sensitivity [$S(\lambda)$] is defined as^[42,43]

$$S(\lambda) = \frac{\Delta\lambda}{\Delta n_{\text{ana}}} \text{ (nm/RIU)}, \quad (12)$$

where $\Delta\lambda$ is the wavelength shift, and Δn_{ana} is the RI variation. The RI resolution (R) of the sensor is defined by^[42,43]

$$R = \Delta n_{\text{ana}} \Delta\lambda_{\text{min}} / \Delta\lambda = \Delta\lambda_{\text{min}} / S(\lambda), \quad (13)$$

where the wavelength resolution can be supposed as $\Delta\lambda_{\text{min}} = 0.1 \text{ nm}$ for most spectrometers.

The amplitude sensitivity (S_A) is expressed as^[42,43]

$$S_A(\lambda) = -\frac{1}{\alpha(\lambda, n_{\text{ana}})} \frac{\partial \alpha(\lambda, n_{\text{ana}})}{\partial n_{\text{ana}}} \text{ (RIU}^{-1}\text{)}, \quad (14)$$

where λ is the resonance wavelength, n_{ana} is the RI of the analyte, $\alpha(\lambda, n_{\text{ana}})$ denotes the overall loss, $\partial \alpha(\lambda, n_{\text{ana}})$ is the difference of two adjacent loss spectra at the given λ and n_{ana} , and ∂n_{ana} is the analyte RI variation. The figure of merit (FOM) of the sensor can be expressed as^[55,56]

$$\text{FOM} = \frac{\eta(\text{eV} \cdot \text{RIU}^{-1})}{\text{FWHM}(\text{eV})}, \quad (15)$$

where η is the slope of the resonance wavelength versus RI, and FWHM is the full width at half-maximum of the loss spectrum.

Many plasmonic PCF-SPR structures have been simulated by various methods, and the finite element method (FEM) is the most common method to compute the optical properties of PCF-SPR sensors. By means of FEM, Hassani *et al.*^[57] have investigated the sensitivity of two PCF-SPR sensors with/without defects with respect to the variation in the thickness of the Au–Ag layer deposited onto the fiber surface, as shown in Fig. 4. In the simulation, the perfectly matched layers (PMLs) are employed to obtain the complex propagation constants, confinement losses, and dispersion curves of the core-guided mode and plasmonic mode. Figure 4 shows that introduction of a structural defect into the PCF cross section near the Au layer allows one to tune the relative position of the two plasmonic peaks. The FEM-based commercial COMSOL software is commonly implemented to investigate the guiding properties and sensing performance of the sensor, and the RF module and wave optics module in the COMSOL software are mainly employed in two-dimensional (2D) simulation of PCF-SPR sensors. Because an extra-fine mesh size is required, the number of vertices in the structure and minimum element quality should be considered as well. The free triangulation can be chosen to divide the mesh size for PCF simulations due to the precise division, which further minimizes computational errors and ensures the accuracy of the results.

Although SPR simulation can be carried out by means of Rsoft, Opti-FDTD software based on the finite-difference time-domain (FDTD) method, FDTD requires solving the partial differential equations in the time domain, consequently

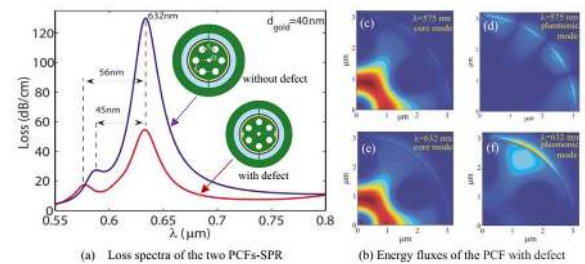


Fig. 4. (a) Loss spectra of two PCFs with and without defect. (b) Electronic field distributions of the PCF with defect: insets (c) and (d) show the electronic field distributions of the fundamental core-guided mode and higher-order plasmonic mode at $\lambda = 575 \text{ nm}$; insets (e) and (f) show the energy distribution of the fundamental core-guided mode and fundamental plasmonic mode at $\lambda = 632 \text{ nm}$ ^[57].

requiring a fine mesh and occupying a great deal of computer memory^[47]. On the contrary, FEM is becoming the preferred simulation method due to automated meshing provided by the COMSOL software, which can determine the optical modes with relatively small computer memory requirements. Therefore, it is more common to adopt the FEM-based COMSOL software to simulate PCF-SPR sensors.

3.2. Performance of PCF-SPR sensors

PCF-SPR sensors have attracted considerable interests, and various sensing structures have been demonstrated to deliver excellent sensing performance. The properties are described based on the following categories: (1) RI detection including low/high RIs, (2) controllable resonance wavelength, and (3) extremely high sensitivity.

3.2.1. Low refractive index detection

The distinguishing feature of SPR is extremely high sensitivity to variations in RI of the surrounding medium, and sensing applications of SPR originate from the changes of the RI caused by the measured parameters. Hence, RI monitoring is one of the most significant functions of PCF-SPR sensors and also fundamental to the measurement of other parameters such as temperature, concentration, and magnetic field.

One of the crucial issues for SPR effect excitation is to satisfy phase matching conditions between the fundamental core-guided mode and plasmonic mode. Mathematically, phase matching is fulfilled when the effective RIs of the above-mentioned two modes are equal at a given wavelength. Generally, the effective RI of the fundamental core-guided mode in a PCF is close to that of the silica core, which is higher than 1.45 in practical applications. According to the Eq. (1), the real part of the effective RI of the SPW is approximately close to that of the surrounding medium^[37,52,57]. Therefore, it is relatively easy to excite SPR for the analyte when the RI of the analyte is close to that of the fiber core. Although most PCF-SPR sensors aim at analyte detection with an RI around 1.33, there is a great demand for PCF-SPR sensors for low RI detection in chemical and biological analysis, including halogenated alkyl ethers, fluorinated organics, liquid carbon dioxide, aerogels, and so on.

Generally, the upper limit of RI detection for a PCF-SPR sensor is less than or equal to 1.33, and it is defined as a low RI sensor. At present, there are many applications available that need to detect a lower RI, such as aerogel^[58], halogenated ether^[59], sevoflurane^[60], and pharmaceutical drugs^[61]. In order to broaden the RI detection range, a PCF-SPR probe coated with Au nanowires has been reported to monitor the low RI of 1.27–1.36^[62]. The probe possesses one large-size microfluidic channel, which can avoid channel interference with each other. Additionally, a dual-side-polished D-shaped PCF has been firstly reported, to the best of our knowledge, to enable low RI detection of 1.23–1.29 in the mid-infrared wavelength region of 2550–2900 nm. Two large air holes in the PCF are formed to be opening rings coated with Au layers as the analyte

channels^[63]. The resonance spectra depend on the size of the incision and exhibit tunability with the size change from 0.872 μm to 1.428 μm . The average wavelength sensitivity of the sensor reaches 5500 nm/RIU over all of the RI range of 1.23–1.29, corresponding to a maximum resolution of 7.69×10^{-6} RIU. Figure 5 displays the electronic field distributions of different modes in the sensor. The largest energy is transferred from the core-guided mode to the plasmonic mode when both modes are strongly coupled.

Haque *et al.*^[64] proposed a D-shaped PCF sensor based on SPR for a wider low RI range of 1.00–1.37, and the homologous cross section of the sensor is shown in Fig. 6(a). Plasmonic Au is used to coat the top surface of the polished side with a TiO₂ layer between the Au and silica glass. Apart from being an adhesive agent, TiO₂ enhances the resonance effect between the core-guided fundamental and SPP modes. The fundamental property of achieving the phase matching coupling point is explained in Fig. 6(b). This side-polished structure coated with the composite film is more beneficial to the detection of low RI analytes, as shown in Figs. 6(c) and 6(d). Zeng *et al.*^[65] designed a D-shaped PCF sensor based on SPR for low RI monitoring. The D-shaped structure coated with two Au nano-belts reduces the coating area and facilitates coupling between the fundamental core-guided mode and plasmonic mode. The enhanced birefringence

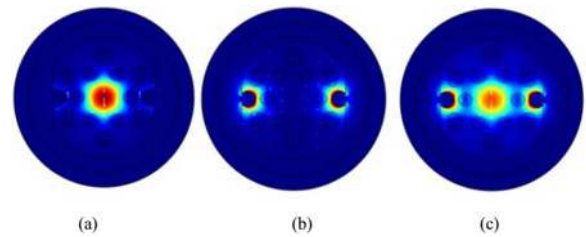


Fig. 5. Electronic field distributions of the sensor for different modes: (a) for the core-guided mode, (b) for the plasmonic mode, and (c) for the two modes at resonance point^[63].

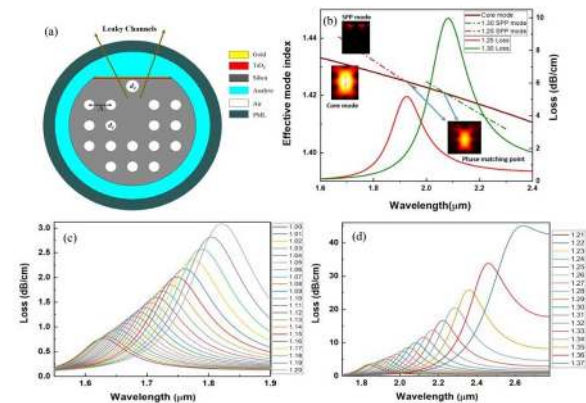


Fig. 6. (a) Schematic illustration of the side-polished sensor. (b) Dispersion relations and loss spectra of the sensor. (c) Resonant curves for RIs of 1.00–1.20. (d) Resonant curves for RIs of 1.21–1.37^[64].

causes a larger evanescent field in the y -polarized mode. This sensor shows a maximum wavelength sensitivity of 12,600 nm/RIU in the RI range from 1.15 to 1.36. Chen *et al.*^[60] investigated a D-shaped PCF sensor based on the SPR effect, and a large opening ring air hole coated with a 50-nm-thick Au film is used as the analyte channel. This structure integrates advantages of a side-polished surface and opening ring channel, not only reducing the area of Au thin film, but simplifying fabrication complexity, thereby enhancing the SPR coupling effect. By optimizing structural parameters, the RI detection range of the sensor is 1.20–1.29. A maximum wavelength sensitivity of 11,055 nm/RIU is obtained, corresponding to a high resolution of 9.05×10^{-6} RIU. Recently, a series-wound PCF-SPR sensor coated with dual Au nanowires was proposed^[39]. In this structure, two Au nanowires are attached on the cladding surface of two adjacent fibers rather than infiltrating into air holes in the PCF. Owing to the dual-core structure, the even mode and odd mode are excited concurrently for both x polarization and y polarization. A maximum spectral sensitivity of 17,500 nm/RIU is achieved in the RI range from 1.13 to 1.35, corresponding to a resolution as high as 5.71×10^{-6} RIU. These reported sensors exhibit a promising potential for monitoring biochemical dynamics and environment pollutions due to ultrahigh sensitivity and fabrication simplicity^[66].

3.2.2. High refractive index detection

The lower limit of RI detection greater than 1.33 is referred to high RI PCF-SPR sensing. High RI detection is useful in determining chemo-analytes and bio-analytes such as polymethylphenyl siloxane, glucose, benzene, and DNA^[67–69]. In practical applications, the biochemical analyte is dissolved in a liquid by an antigen-antibody interaction or protein-DNA/RNA binding process. The molecular interactions of DNA can be detected by a poly-L-lysine bound surface, which generally has an RI range of 1.45–1.48. Chu *et al.*^[68] proposed a two-channel PCF-SPR sensor for multi-sensing, as shown in Fig. 7. This sensor constitutes a D-shaped dual-core six-fold PCF and two Ag nanowires placed on the two channels. As shown in Fig. 7(c), the resonance wavelengths for the two sensing channels are determined to be 697 nm and 780 nm, respectively. Figure 7(d) presents the light energy flow distributions of the fundamental core-guided mode and SPP mode. The biosensor exhibits a maximum RI sensitivity of 3400 nm/RIU and a resolution of 2.94×10^{-5} RIU for a large sensing range from 1.35 to 1.50, which covers most known analytes such as proteins, viruses, and DNA/RNA. Recently, graphene-modified SPR sensors have attracted much attention due to strong pi-stacking forces and specific interaction^[70,71]. Coating graphene layers on Au or Ag thin films can induce larger SPR signal changes compared to bare metal thin films. This is mainly due to charge transfer from graphene to the surface of metal thin film since the work function is different, and this effect leads to strong excited electric field enhancement on the sensor surface^[71].

Besides graphene, semiconductor oxide-TiO₂ has also obtained great attention due to the enhancement for the SPR

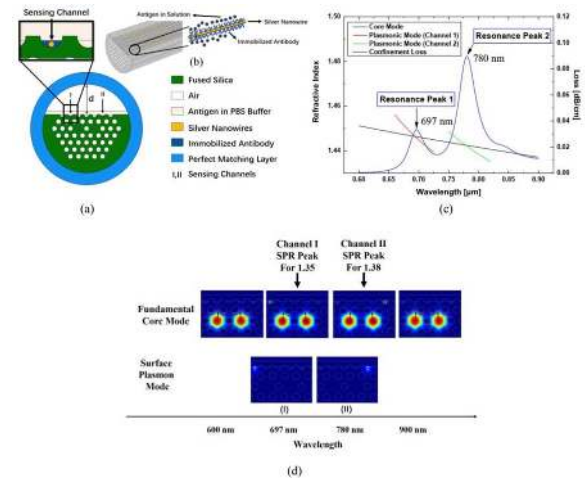


Fig. 7. (a) 2D diagram of the sensor. (b) Three-dimensional (3D) diagram of the sensor. (c) Dispersion relations and loss spectrum of the sensor (red line represents channel 1 for $n_a = 1.35$, green line represents channel 2 for $n_a = 1.38$). (d) Electric field distributions of the sensor for different wavelengths^[68].

effect^[51,72]. De *et al.*^[73] simulated a flat fiber plasmonic sensor with a Au-TiO₂ coating by FEM. The Au-TiO₂ bi-layers act as SPR sensitive materials, which are deposited onto the upper flat surface of the fiber. The sensor possesses an average wavelength sensitivity of 12,172 nm/RIU in an RI range of 1.445–1.490, corresponding to a sensing resolution of 8.21×10^{-6} RIU. In addition, this sensor also has an amplitude sensitivity of 2910 RIU⁻¹ with a resolution of 3.44×10^{-6} RIU. These excellent sensing performances are mainly attributed to the introduction of transparent TiO₂ layers with a high RI, which contributes to coupling of the core-guided mode to the plasmonic mode. Gandhi *et al.*^[74] reported a D-shaped PCF micro-biosensor based on the local SPR effect, as shown in Fig. 8. The Au layer, Au-TiO₂ bi-layer, or Au-TiO₂-grating is coated on the D-shaped PCF surface. This sensor can enable a wide RI detection range of 1.33–1.45 and a wide operating wavelength range of 500–2000 nm. An *et al.*^[75] proposed a PCF-SPR sensor for an extra-broad RI monitoring. The PCF consists of a triangular lattice and four large-size channels. The RI detection ranges from 1.30 to 1.79, and the operating wavelength can be adjusted in the range of 1680–1870 nm, which is the largest high RI detection range reported so far. On the heels of the continuous development of microstructured PCF-SPR sensors, a large number of PCF-SPR sensors have been

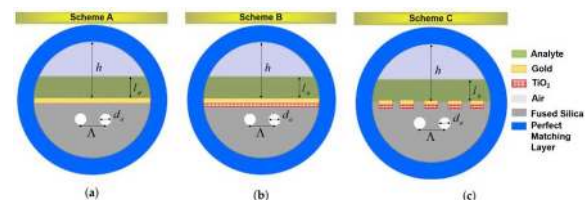


Fig. 8. Schematics of the 2D cross section: (a) coated with an Au layer, (b) coated with Au and titanium dioxide layers (TiO₂), and (c) coated with the Au-TiO₂ grating^[74].

designed to detect low or high RI substances, and a summary of the PCF-SPR sensors is shown in Table 1. It is seen from Table 1 that PCF-SPR sensors with various structures are applicable for RI detection and possess relatively high maximum wavelength sensitivities. The smallest detectable RI is as low as 1.0, while the largest detectable RI is up to 1.79. It is noted that excellent sensing performances are essentially determined by PCF-SPR structures and sensitive materials.

It should also be noted that numerous D-shaped PCF-SPR sensors have drawn growing attention because of their unique shapes^[50,60,72,76], exhibiting great practical application potentials in RI sensing. The D-shaped fibers provide a flat plane to deposit plasmonic materials easily, which can be prepared by the side polishing technique^[41,65,70,74]. The plasmonic materials such as multilayered composite films, nanoparticles, and gratings can be coated adjacent to the fiber core to promote strong interactions between the fundamental mode and plasmonic mode, thus enhancing the sensing performance and realizing low/high RI detection^[77–79].

3.2.3. Broad resonance wavelength detection

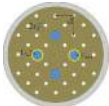




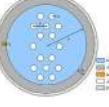
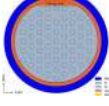



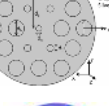
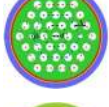

SPR is an optical phenomenon involving resonance excitation of a total internal reflection evanescent wave coupled with free electron collective oscillations in the surface of plasmonic materials. According to the aforementioned confinement loss formula, PCF-SPR exhibits the maximum loss intensity at the resonance wavelength corresponding to surface plasmons. Consequently, this resonance wavelength is one of the key concepts in SPR and can be tuned if the RI of the surroundings is varied by adjusting the geometric parameters of PCF-SPR. The shift of the resonance wavelength can be used to sense parameters that produce slight variations in the RI boding well for sensing applications. In reported literatures, most PCF-SPR sensors have been used for the visible and near-infrared wavelength region^[37,52] due to the wide availability of light sources. To extend the application of SPR sensing to larger biomolecules, it is necessary to increase the SPW probing depth, implying that longer resonance wavelengths are required. Therefore, a large controllable resonance wavelength range is desirable for PCF-SPR sensors.

Miniaturized sensors with a simple structure, quick response, and wide wavelength range have been proposed. An *et al.*^[80] presented a quasi-D-shaped PCF-SPR biosensor, as shown in Fig. 9(a). The plasmonic materials consist of metal oxide ITO and graphene. The operating wavelength can be controlled in the near-infrared range from 1500 nm to 2500 nm for RI sensing. The computational results show that a maximum wavelength sensitivity of 10,693 nm/RIU can be achieved with the corresponding resolution of 9.35×10^{-6} RIU. Liu *et al.*^[81] developed a side-core PCF-SPR sensor with a Ag core, as shown in Fig. 9(b). Compared with the structure of an analyte hole coated by a nano-metal layer, different sensing properties are observed. This structure not only is a dual-core microstructure, but also exhibits the special phenomenon where *y*-polarized light facilitates detection by resonance-based RI sensing using a side core

in the *x* direction. The structure enhances the overlapping area of the core and SPP modes giving rise to a maximum sensitivity of 23,821 nm/RIU in the wavelength range of 700–2800 nm. Haider *et al.*^[82] analyzed a simple PCF structure-based SPR sensor, as shown in Fig. 9(c), which is capable of detecting external analytes. Hence, detection of analytes can be carried out by streaming them through the Au surface or simply keeping them on the surface. The sensor operates in the wavelength range of 500–1400 nm and possesses a high amplitude sensing response of 2843 RIU⁻¹. Liu *et al.*^[83] described a PCF-SPR structure with ITO as the sensitive material [Fig. 9(d)]. Compared to Au and Ag, ITO is cheaper for SPR excitation. The ITO thin film can be easily fabricated on the surface of the photonic quasi-crystal fiber (PQF) by conventional coating methods such as chemical vapor deposition. The theoretical wavelength sensitivity of the sensor reaches 21,100 nm/RIU at the operating wavelength between 1400 nm and 2200 nm, and the average wavelength sensitivity is up to 8750 nm/RIU.


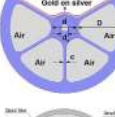
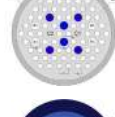
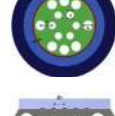

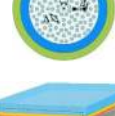
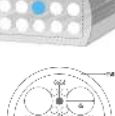

Figure 9(e) presents a twin-core PCF plasmonic RI sensor boasting a wavelength range from 1400 to 2200 nm. The wavelength interrogation method determines the maximum wavelength sensitivity of around 9000 nm/RIU for both the *x*- and *y*-polarized modes^[84]. Due to the fact that Ta₂O₅ has a low waveguide loss of 1 dB/cm at an infrared wavelength, high transparency in a wide spectrum, and the high fusion point, it is enabled as a commendable material for fiber sensors^[85,86]. Li *et al.*^[87] designed a high-sensitivity RI sensor [shown in Fig. 9(f)] based on Au-Ta₂O₅ bilayered-coating PCF-SPR at the near-infrared wavelength range of 1100–1700 nm. In addition, the Au and Ta₂O₅ layers in the large container air holes in the vertical direction show large differences between the liquid containing holes and other holes in the fiber structure. Unlike the D-shaped structures or small coating holes and liquid-filling fiber core PCFs for high RI sensing, this sensor possesses a simple, pure silica solid core structure and offers more convenience in the arc discharge pre-treatment. Recently, a PCF-SPR sensor with two opening rings as analyte channels described in Fig. 9(g) has been designed^[63]. The inner walls of the opening rings are coated with the Au film with a thickness of 42–50 nm, and the analyte can enter the opening rings through the open slots automatically. The size of the open slots is controllable by manipulating the side-polished depth, enabling the selective detection function. The maximum wavelength sensitivity is 5500 nm/RIU, and the amplitude sensitivity is 333.8 RIU⁻¹, in addition to a sensing resolution of 7.69×10^{-6} RIU. In this way, the resonance wavelengths of this sensor are tuned to the mid-infrared wave band from 2550 nm to 2900 nm. Figure 9(h) presents the schematic illustration of a unique PCF-SPR sensor^[58]. This sensor constitutes two parallel D-shaped PCFs coated with a Au layer and operates at near-infrared wavelengths. According to the coupled-mode theory, directional power transfer between the two fiber cores is enhanced by resonant coupling between the surface plasmon modes and fiber core-guided modes^[88,89]. In comparison with the corresponding single D-shaped PCF, a maximum spectral sensitivity of 13,500 nm/RIU and a

Table 1. Refractive Index Ranges of Recently Reported Sensors.

Ref.	Characteristic	Refractive Index Range	Max. Sensitivity (nm/RIU)	Resolution (RIU)	Str. Diagram
[88]	Birefringence PCF	1.00–1.43	6300	1.58×10^{-5}	
[76]	D-shaped PCF	1.18–1.36	20,000	5.00×10^{-6}	
[90]	Concave-shaped PCF	1.19–1.29	10,700	9.34×10^{-5}	
[60]	D-shaped PCF	1.20–1.29	11,055	9.05×10^{-6}	
[66]	Microchannel PCF	1.22–1.37	51,000	1.96×10^{-6}	
[62]	Gold-nanowire-coated PCF	1.27–1.36	6000	2.8×10^{-5}	
[77]	D-shaped PCF	1.27–1.32	10,493	9.53×10^{-6}	
[91]	Gold-coated PCF	1.29–1.49	4156	2.41×10^{-5}	
[92]	PCF with circular air holes	1.32–1.43	30,500 (x), 41,500 (y)	3.28×10^{-6} (x), 2.41×10^{-6} (y)	
[40]	PCF with exposed core	1.33–1.42	13,500	7.41×10^{-6}	
[78]	Graphene-based D-shaped PCF	1.33–1.37	3700	2.7×10^{-5}	
[93]	Copper-graphene-based PCF	1.33–1.37	2000	5.0×10^{-5}	
[94]	External gold-layer-coated PCF	1.33–1.37	4000	2.50×10^{-5}	

(Continued)

Table 1. (Continued)

Ref.	Characteristic	Refractive Index Range	Max. Sensitivity (nm/RIU)	Resolution (RIU)	Str. Diagram
[95]	Hexagonal sensor	1.33-1.42	11,000	9.10×10^{-6}	
[96]	PCF with exposed core	1.33-1.42	16,400	6.1×10^{-6}	
[97]	Au-coated dual-core PCF	1.33-1.51	6021	1.66×10^{-5}	
[98]	Hollow core Ag-coated PCF	1.36-1.37	4200	2.38×10^{-5}	
[79]	D-shaped PCF coated with gratings	1.36-1.38	3340	Not applicable	
[99]	Eight-fold eccentric core PQF	1.38-1.413	96,667	1.034×10^{-6}	
[100]	Flattened PCF	1.49-1.54	4782	2.09×10^{-5}	
[75]	Four large channels	1.63-1.79	3233	3.09×10^{-5}	

resolution of 7.41×10^{-6} RIU are achieved for the wavelength range between 720 and 1680 nm. The parallel D-shaped PCF-SPR sensor has large potential in pharmaceutical inspection and pharmaceutical leakage monitoring.

Plasmonics technology has been improved, and more PCF-SPR sensors are produced to operate in different wavelength ranges. A comparison of recently reported PCF-SPR sensors and their characteristics are presented in Table 2. The resonance wavelength in various PCF-SPR sensors can be easily tuned to the near-infrared or mid-infrared region from the visible region by means of optimizing PCF structures and plasmonic materials such as Au, Ag, graphene, and ITO. In addition, it is worth noting that D-shaped PCF-SPR sensors exhibit particular flexibility in resonance wavelength tunability.

3.2.4. Extremely high-sensitivity detection

The demand for SPR-based sensors with higher sensitivity, better precision, and faster response is increasing. In this respect, high sensitivity is one of the goals in the design and fabrication of PCF-SPR sensors. The spectral sensitivity and amplitude

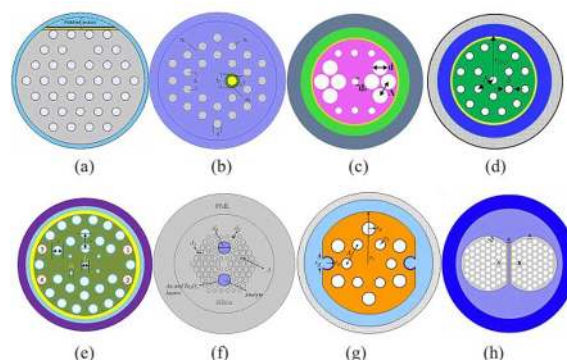
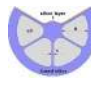
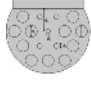

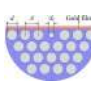
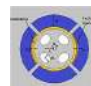



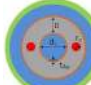


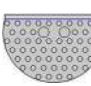



Fig. 9. Typical cross-sectional views of various PCF-SPR sensors. (a) Graphene over ITO coated PQF^[80]; (b) a Ag core^[81]; (c) hexagonal structure consisting of two air hole rings with a central air hole^[82]; (d) eccentric core PQF with ITO coating^[83]; (e) twin-core PCF with Au coating^[84]; (f) analyte filling with Au-Ta₂O₅ coating^[87]; (g) two open-ring channels with Au coating^[63]; (h) two parallel D-shaped structures^[58].

Table 2. Comparison of the Wavelength Ranges of Recently Reported Sensors.

Ref.	Characteristic	Wavelength Range (nm)	Max. Sensitivity (nm/RIU)	Resolution (RIU)	Str. Diagram
[40]	PCF with exposed core	460–620	13,500	/	
[78]	Graphene-coated D-shaped PCF	480–650	3700	2.7×10^{-5}	
[101]	Hollow core PCF with silver nanowires	560–610	14,240	/	
[50]	Hollow core D-shaped PCF	550–750	2900	/	
[86]	Multichannel PCF	550–950	4600	2×10^{-5}	
[72]	D-shaped PCF	550–1770	46,000	2.2×10^{-6}	
[102]	Dual-core PCF	600–1200	28,000	3.57×10^{-6}	
[103]	Square array PCF	630–1180	7250	1.38×10^{-5}	
[104]	Bilaterally gold-coated PCF	1000–3400	30,000	3.33×10^{-6}	
[41]	ITO-coated D-shaped PCF	1200–2250	15,000	6.67×10^{-6}	
[83]	PCF with eccentric core	1400–2200	21,000	4.74×10^{-6}	
[105]	ITO-coated D-shaped PCF	1870–2300	17,000	5.8×10^{-6}	
[60]	D-shaped PCF with open ring	2300–2850	11,055	9.05×10^{-6}	

sensitivity are employed to evaluate the sensing characteristics, and the performance is affected by the air hole arrangement, plasmonic materials, and layer thickness. Highly sensitive sensors can be designed by optimizing the structural parameters and air hole configurations in the PCFs. The plasmonic sensors such as dual-side-polished structures^[106,107], microchannel incorporated D-shaped Au-grating structures^[79], and H-shaped structures^[108] have been innovatively explored by the FEM-

based COMSOL Multiphysics software. Owing to the convenient simulation software, the sensing performance of the sensors with complicated structures can be numerically calculated. Among them, the PCF-SPR sensor with U-shaped grooves coated with Ag-graphene exhibits a maximum spectral sensitivity of 12,600 nm/RIU in the RI range of 1.33–1.41^[108]. Graphene protects Ag from oxidation, and these side-polished structures have advantages such as easy coating with Au films and outside

sensing channels, rendering them ideal in real-time sensing^[109,110].

Han *et al.* studied a high-sensitivity plasmonic sensor based on an H-shaped PCF^[111]. The H-shaped grooves coated with Au film in the proposed PCF serve as the analyte channels and contact with the analyte directly. The depth and width of the grooves are 34 μm and 4 μm , respectively. It is relatively easy to create this kind of groove structure by using laser ablation and focused ion beams. Therefore, this structure not only reduces the manufacturing process of the sensors, but also provides reusable possibilities compared to other structures. The RI detection of the sensor is 1.33–1.49, and a maximum sensitivity of 25,900 nm/RIU is obtained in the RI range of 1.47–1.48. With regard to the popular D-shaped PCF-SPR sensors, although the maximum spectral sensitivity and average sensitivity increase with the width of the Au film in a certain range, an excessively large width leads to coupling of the core mode and higher-order SPP mode, resulting in multi-peak interference in the detection band affecting the sensing effectiveness. By optimizing the width of the Au film, the diameter of the air holes, and the thickness of the Au film, a maximum spectral sensitivity of 34,000 nm/RIU and an average sensitivity of 10,250 nm/RIU are accomplished^[112]. Recently, an air core PCF-based plasmonic sensor has been investigated by FEM, and the core of the PCF is infiltrated with the analyte through an open-side channel. The spectral sensitivity and resolution are 11,700 nm/RIU and 8.55×10^{-6} RIU, respectively^[113]. In order to improve the detection efficiency, a dual-channel PCF-SPR sensor has been proposed. By optimizing the dielectric layer, the detecting ability of the channels is improved, and the wavelength sensitivities of two simultaneous channels approach 11,600 nm/RIU and 10,600 nm/RIU, respectively^[106]. An octagonal PCF-based SPR RI sensor has been designed to monitor the moisture content in transformer oil, and graphene is used as the plasmonic

material^[114], as shown in Fig. 10. The maximum amplitude sensitivities are 31,240 RIU⁻¹ and 30,830 RIU⁻¹ for the *x*-polarized and *y*-polarized modes, respectively, which are the largest high-amplitude sensitivities reported up to now. The sensor also shows an FOM of 5000. Such highly sensitive sensors exhibit great application potential in demand for monitoring steam quality and biomolecular concentration.

Recently, an RI biosensor comprising a PCF-SPR has been studied, and Au nano-film is selected as the active material^[115]. The thickness of the Au layer has a large impact on the sensitivity. The maximum spectral sensitivity of 45,003.05 nm/RIU is observed for the RI range from 1.33 to 1.40, and the PCF also exhibits a high birefringence of 1.9×10^2 . The extremely high sensitivity makes it suitable for functional biological environments. In addition, a D-shaped PCF-SPR sensor has been designed by introducing TiO₂-Au-graphene hybrid plasmonic materials^[116]. The graphene is deposited on Au film to contribute adsorption of biomolecules on the surface. In their work, a maximum wavelength sensitivity of 48,900 nm/RIU is achieved, and the average sensitivity is up to 13,112.5 nm/RIU over all of the RI range between 1.32 and 1.40. The maximum resolution of the wavelength sensitivity is approximately 7.6×10^{-6} RIU, exhibiting powerful ability to detect small variations of the RI. The sensor presents a high amplitude sensitivity of 738.74 RIU⁻¹ and a maximum FOM of 611.25 RIU⁻¹. The promising outcome renders it a potential sensor for organic and biomolecules. As the aforementioned micro-biosensor with the Au-TiO₂-grating as the plasmonic material^[74], the sensor possesses a maximum wavelength sensitivity of 75,000 nm/RIU in a wide RI range of 1.33–1.45, and the corresponding resonance wavelength ranges from 500 to 2000 nm. The discrete metallic gratings on the D-shaped surface reinforce the LSPR effect and improve electron ionization, consequently resulting in a large mode field distribution and an enhanced spectral sensitivity.

In order to enhance SPR sensitivity, it is fundamentally necessary to improve interaction between the fundamental core-guided mode and plasmonic mode. One of the effective approaches attempted is under the assistance of dual-parallel PCF-SPR sensors. A symmetrical dual-beam D-shaped PCF-SPR sensor has been developed^[89]. The average wavelength sensitivity of 14,660 nm/RIU is achieved in the RI range of 1.36–1.41, and the corresponding resolution approaches 6.82×10^{-6} RIU. As a comparison, they calculated the sensing properties of the single fiber with the same D-shaped structural parameters. The average spectral sensitivity and average resolution of the single D-shaped sensor are 4740 nm/RIU and 2.11×10^{-5} RIU in the RI range of 1.36–1.41. The comparison implies that the average sensitivity of the symmetrical dual D-shaped fiber is three times larger than that of the single D-shaped fiber. Hence, the enhanced sensing performance of the PCF-SPR sensor is mainly attributed to the directional energy coupling between the two fibers. Table 3 compares the characteristics of the selected high sensitivity of recently reported PCF-SPR sensors. It is found from Table 3 that numerous highly sensitive PCF-SPR sensors have been proposed and designed in recent

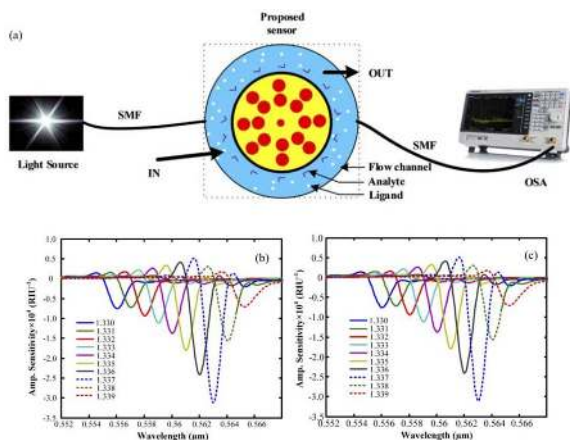


Fig. 10. (a) General setup for practical sensing; (b) amplitude sensitivity curves of the moisture-monitoring sensor for the *x*-polarized mode; (c) amplitude sensitivity curves of the moisture-monitoring sensor for the *y*-polarized mode ($d = 0.76 \mu\text{m}$, $n = 1.330\text{--}1.340$, $d_c = 0.3 \mu\text{m}$, $t_g = 40.12 \text{ nm}$, and $\Lambda = 0.8 \mu\text{m}$)^[114].

Table 3. Comparison of the Characteristics of Selected High Sensitivity of PCF-SPR Sensors Reported Recently.

Ref.	Fiber Type	Refractive Index Range	Wavelength Range (nm)	Max. Sensitivity (nm/RIU)	Resolution (RIU)	Amp. Sensitivity (RIU ⁻¹)	Str. Diagram
[117]	Dual-channel PCF	1.33–1.40	500–1000	11,600	8.62×10^{-6}	N/A	
[113]	PCF with air core	1.33–1.41	800–1700	11,700	8.55×10^{-6}	159.70	
[89]	Dual D-shaped PCF	1.36–1.41	640–1040	14,600	6.82×10^{-6}	1222	
[118]	Multi-analyte PCF	1.34–1.41	560–990	18,000	5.56×10^{-6}	427	
[119]	D-shaped PCF	1.35–1.38	1200–2400	18,900	5.29×10^{-6}	/	
[120]	Gold-coated PCF	1.33–1.40	550–1200	19,000	5.26×10^{-6}	985	
[121]	D-shaped PCF	1.33–13.4	500–900	21,700	4.61×10^{-5}	/	
[122]	TiO ₂ -Au-coated PCF	1.32–1.40	600–1080	23,000	4.34×10^{-6}	/	
[111]	H-shaped PCF	1.33–1.49	800–2000	25,900	3.86×10^{-6}	N/A	
[123]	D-shaped PCF	1.33–1.43	600–1100	31,600	3.16×10^{-6}	550	
[112]	D-shaped PQF	1.415–1.427	1400–1700	34,000	2.94×10^{-6}	N/A	
[115]	Gold-coated PCF	1.33–1.40	1520–1670	48,269	2.07×10^{-6}	N/A	
[116]	D-shaped PCF	1.32–1.40	410–1790	48,900	2.04×10^{-6}	738.74	
[124]	Dual-core PCF	1.29–1.39	1200–3500	116,000	8.65×10^{-7}	2320	

years. The maximum wavelength sensitivity is up to 11,000–116,000 nm/RIU with a higher resolution of 10^{-6} , displaying great application potential in bio-sensing.

3.3. Fabrication of PCF-SPR sensors

PCFs consist of a periodical arrangement of micro-capillaries that form the fiber cladding around a solid or hollow defect core. Fabrication of PCF-SPR sensors involves two aspects of manufacturing PCF and producing plasmonic nanomaterials. Advances pertaining to the manufacturing and post-processing technology of optical fibers have spurred substantial development in techniques such as extrusion, casting/molding, mechanical drilling, and stack-and-draw. The stack-and-draw technique invented by Birks *et al.* in 1996 and shown in Fig. 11 is the most versatile and flexible fabrication technique for PCFs due to the remarkable advantage of flexible preform manufacturing^[125]. The PCF preform consists of dozens of capillary silica tubes and rods in terms of the desired structure. After the fabrication of the preform, it is necessary to draw down the preform size by using an optical fiber drawing tower, remarkably extending the preform length while keeping the cross-sectional diameter decreased from 20 mm to 80–200 μm . The stack-and-draw method offers advantages such as the low cost and flexibility to fabricate a large variety of PCFs for different applications. However, it is not easy to produce high-quality plasmonic nanomaterials inside the PCF, and there are alternative methods to prepare plasmonic materials.

3.3.1. Infiltration of plasmonic materials into PCF

PCF-SPR involves coupling between the fundamental core-guided mode and plasmonic mode. In order to obtain excellent sensing properties, the alternative approach is to enhance the interaction between the two modes by controlling the distance between them. One strategy is to introduce plasmonic materials such as nanowires, nanofilms, and nanoparticles into the air channels in PCFs. High-pressure chemical vapor deposition (HPCVD) suggested by Sazio *et al.*^[126] in 2006 provides an effective technique for nanomaterial infiltration into the channels of PCFs. The air holes in the PCFs can be regarded as chemical micro-reactors, in which nanoscale materials such as Ag and

Au are deposited onto the inner walls of air holes. Figure 12(a) presents the schematic illustration of HPCVD, and Fig. 12(b) displays the image of hexagonal Si tubes in a PCF. Figure 12(c) presents an image of a Au nanoparticles array within a 1.6 μm diameter capillary. Figure 12(d) displays the formation of an 80-nm-thick Au film on a Si tube. Based on the HPCVD technique, Au, Ag, and other plasmonic materials can be successfully grown on the inner walls of air holes inside PCFs, realizing a customized film function.

PCF-SPR sensors have benefited from high-pressure chemical deposition by coating plasmonic nanoparticles (Au, Ag) inside the holes of PCFs. However, the high-pressure (10–100 MPa) environment and additional heat treatment with a temperature of 200°C are generally required, which will have adverse effects on the mechanical stability of the fiber. The metal layer is realized only for the length of 15 cm with an approximately 50 μm channel diameter and after a 2 h incubation period. In addition, such a particle coating is homogeneous for 5–6 cm in the middle section of the PCF, since covering gradients are induced by depletion of particles. In 2010, Csaki *et al.*^[127] reported a cost-effective and innovative nanoparticle-layer deposition technique for preparation of well-defined Au nanoparticles inside the channels of PCFs with a suspended-core structure, as shown in Fig. 13. This method utilizes a combination of microfluidics and the self-assembled monolayer technique, leading to

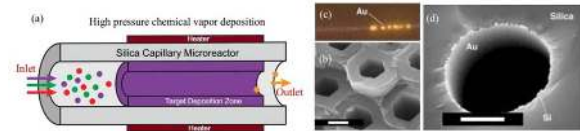


Fig. 12. (a) Schematic illustration of HPCVD. (b) Si tubes in a PCF (scale bar: 1 mm). (c) Image of Au nanoparticles array within a 1.6 μm capillary. (d) Image of Au film grown on the inner wall of the Si tube inside PCF (scale bar: 2 μm)^[126].

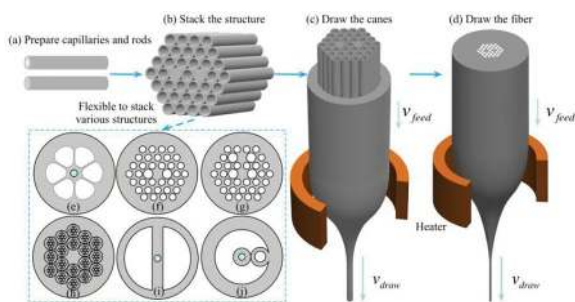


Fig. 11. Illustration of the stack-and-draw method for PCF fabrication^[125].

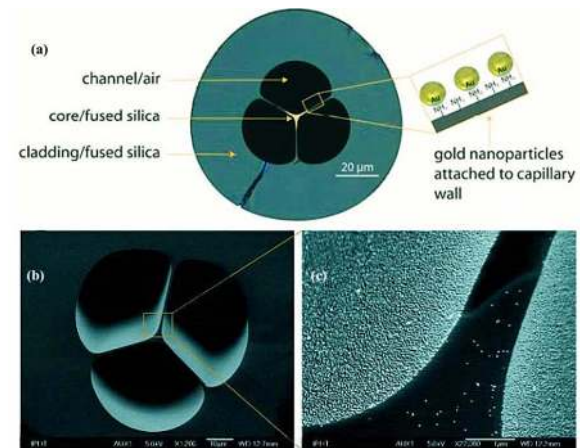


Fig. 13. (a) Schematic of suspended-core fiber front view with Au nanoparticles coating. (b) and (c) SEM images of the inner walls of the suspended-core fiber coated with Au nanoparticles (30 nm diameter spheres): (b) an overview and (c) a zoomed image^[127].

a longitudinal homogeneous particle density as long as several meters. A sensitivity of a 30 nm Au-particle-modified suspended-core fiber is determined to be approximately 78 nm/RIU. By depositing the metallic layers and/or semiconductors inside PCFs, the functionalized PCF can be engineered to exhibit optical properties and application ranges of RI sensing and surface-enhanced Raman spectroscopy^[128–130]. Zhang *et al.* proposed a large suspended-core PCF-SPR sensor, and the Ag layer as the sensitive material is prepared by using the dynamic chemical liquid phase deposition method^[131]. Figure 14 depicts the structure and cross-section images of the fiber with a 700 μm outer diameter. A liquid phase deposition method is employed to coat the Ag layer on the inner surface of the fiber. The ammoniated Ag solution is prepared by mixing 5% AgNO_3 solution with equal volumes of 4% KOH solution and 25% $\text{NH}_3 \cdot \text{H}_2\text{O}$ of an appropriate volume. The reducer is a 5% glucose solution. The coating process can be completed within 2 min. The morphologies of the Ag interface adjacent to the silica fiber core are shown in Figs. 15(a)–15(c), which reveal that the Ag-layer thicknesses of the three fibers are about 54 nm, 66 nm, and 83 nm, respectively. The sensor coated with 83-nm-thick Ag exhibits a higher sensitivity of 2664 nm/RIU, which is approximately 10 times larger than those of suspended-core fiber sensors with metal nanoparticle functionalization. The sensor has the same order of magnitude sensitivity as conventional solid-core fibers and hollow core SPR sensors.

Due to a smaller effective modal scattering area of the suspended-core fiber, it is regarded as an excellent platform with regard to sensing. Doherty *et al.* investigated the nanoparticle-functionalized suspended-core fiber that can be applied to the highly integrated opto-fluidic platform for efficient RI sensing^[132]. The schematic of the suspended-core fibers containing immobilized plasmonic nanoparticles surrounding the core is depicted in Fig. 16. The Au nanoparticle densities are controlled

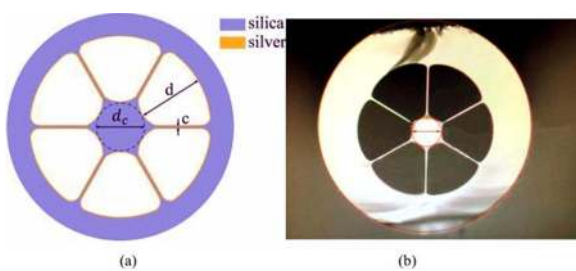


Fig. 14. (a) Structure of the SPR sensor and (b) microscopic image of the cross section of the fabricated suspended-core fiber^[131].

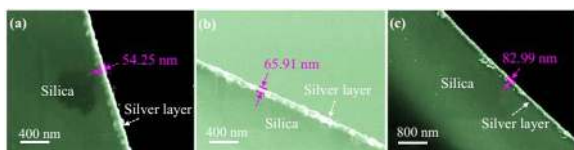


Fig. 15. SEM images of the cross section of the sputtered fibers^[131]. (a) for ~ 54 nm Ag film, (b) for ~ 66 nm Ag film, and (c) for ~ 83 nm Ag film^[131].

by nanoparticle-layer deposition, which is dynamic low-pressure chemical deposition combined with modification of the interior channel surfaces as adhesive layers for the Au nanoparticles^[127,133]. The SPR film is formed when the Au nanoparticle solution is introduced through the inner wall of the functionalized channels at a small flow rate. The dependency of the resonance wavelength shift on the analyte RI is obtained for a density of 22 Au nanoparticles/ μm^2 and a fiber length of 4 mm. The RI sensitivity of the sensor is measured to be 167 nm/RIU for an aqueous analyte when the fiber interior is functionalized with Au nano-spheres. The fundamental working principle of Au nanoparticle-enhanced suspended-core fibers relies on the coupling effect of the propagating core-guided mode with the local SPR of Au nanoparticles.

The micro-holes inside PCFs can be infiltrated with plasmonic nanomaterials including Au, Ag, graphene, and TiO_2 to excite the SPR to broaden the potential application of sensors. Molten Au can be infiltrated into air holes in PCFs by the pressure-assisted method^[134], and Fig. 17 shows the procedure of the spliced-fiber pressure-filling method. After fabricating the silica capillary (outer/inner radius: 100/40 μm) by the optical fiber drawing process, a 2-cm-long Au wire (radius: 25 μm) is inserted manually into the silica capillary, leaving a fresh and clean end face for slicing. The end portion of the silica capillary is cleaved

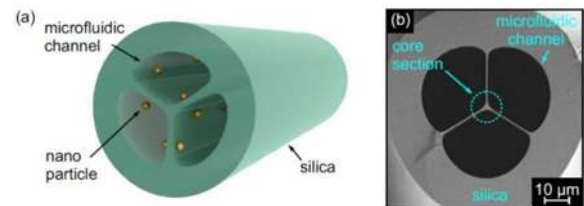


Fig. 16. (a) Schematic of the plasmonic nanoparticle-functionalized suspended-core fiber and (b) SEM image of the microstructured section of the fiber^[132].

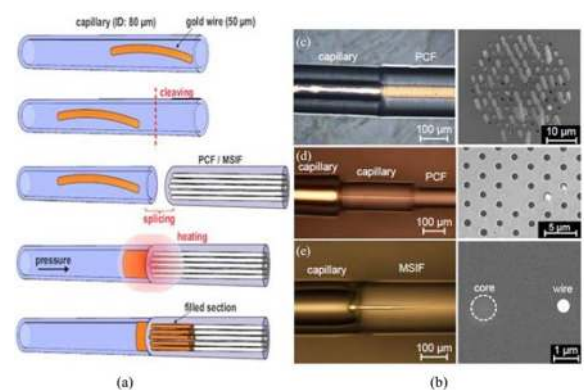


Fig. 17. (a) Spliced-fiber pressure-filling technique and (b) optical side views of the splices (left-hand column) and SEM images of the cleaved end-faces (right-hand column); (c) solid-core PCF with all its channels filled with Au, (d) PCF in which only two channels are filled with Au, (e) modified step index fiber with a parallel Au nanowire^[134].

and spliced into a silica PCF by a splicing machine. By carefully adjusting the splicing parameters, the fiber is placed in a vertical furnace with the spliced section in the center and heated to the Au melting temperature. Argon gas is introduced to a pressure of several hundred bars to push the molten Au into the second end of the capillary. The important condition is that the Au plug and hollow channels in the PCF are in perfect alignment. The typical optical micrographs and scanning electron microscopy (SEM) images of the fibers are shown in Fig. 17(b). For instance, a solid-core PCF with the air hole radius of 0.5 μm and air hole pitch of 3 μm can be completely filled with Au under the pressure of 50 bar, as shown in Fig. 17(c). The spliced-fiber pressure-filling technique is appropriate for non-wetting materials such as Au, Ag, Ga, Ge, as well as chalcogenide glasses^[135,136], which have melting temperatures lower than the softening temperature of silica. The splice-filling technique is more flexible and safer, thus facilitating filling of the selective channels compared to the pressure-cell-filling technique^[137–140]. Nanowires can also be integrated into optical fibers by the co-drawing method to pump metals into the hollow channels of PCFs in the plasmonic fiber structure. Tuniz *et al.* have reported drawn metamaterials comprising microstructured indium-filled polymethylmethacrylate (PMMA) fibers^[141]. Markos *et al.* prepared a hybrid polymer-chalcogenide PCF with integrated As_2S_3 glass nanofilms at the inner surface of the air channels of the PMMA PCF^[142].

3.3.2. Preparation of plasmonic materials on PCFs

From the perspective of fabrication of PCF-SPR sensors, it is easier and more convenient to deposit plasmonic layers on the outside of the PCFs compared to coating plasmonic materials onto the inner wall of air holes of the PCFs. Therefore, the partial cladding is etched or side-polished to enhance the evanescent field for SPR excitation. Wang *et al.* have theoretically and experimentally studied a PCF sensor based on SPR^[121]. An endlessly single-mode (ESM)-12 PCF with a hexagonal structure is selected, which is an all-glass endless SMF with a standard cladding diameter of 125 μm . The ESM-12 fiber is side-polished to be D-shaped and coated with a sputtered Au thin film with a thickness of 45 nm. During side polishing, an additional weight is applied to straighten the PCF and provides a compatible polishing force to increase the polishing speed and system stability. The cross-section and side-polished plane of the D-shaped PCF are shown in Figs. 18(a)–18(e). A spectral sensitivity as high as 21,700 nm/RIU is obtained for the RI between 1.33 and 1.34. Additionally, graphene can enhance the evanescent field to excite SPR in the presence of Au thin film. A similar PCF-SPR sensor structure and the microscopic images are shown in Fig. 19^[143]. A 35-nm-thick Au thin film is successfully fabricated on the exposed core of the PCF by electron beam evaporation. The exposed core fiber is coated with the Au film and graphene at the notch, and the liquid to be measured covers graphene. Owing to the feasibility of different transfer methods of graphene, graphene is coated on the PCF by the pull-up method. The concentration of graphene (1–10 layers) in ethanol dispersions is 1 mg/mL in the experiment. Consequently, a sensitivity

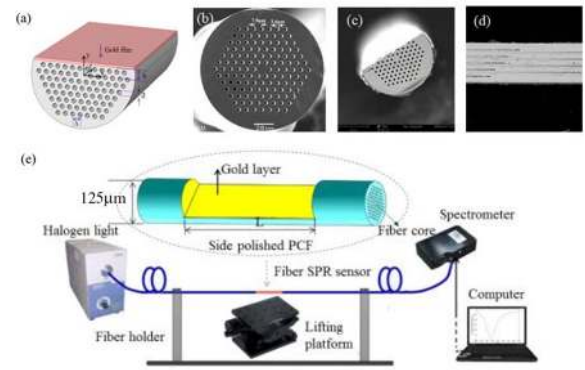


Fig. 18. (a) D-shaped model. (b) SEM image of the PCF before polishing. (c) Cross section of the Au-coated D-shaped PCF. (d) Side-polished surface of the D-shaped PCF with a Au coating. (e) Schematic diagram of the real-time online measurement system^[121].

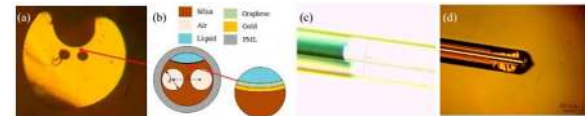


Fig. 19. (a) Structure of the sensor. (b) Schematic diagram of the simulated model. (c) Transmitted light microscopic image. (d) Reflected light microscopic image^[143].

improvement of 390 nm/RIU is obtained due to graphene introduction.

PCFs can be coated with plasmonic nanoparticles, and the SPR response and detection sensitivity can be significantly enhanced by the electric field coupling effect between the metal nanoparticles and PCFs^[144]. Wang *et al.*^[145] proposed an optical fiber biosensor based on Au nanoparticles and protein, and a co-modified Au-film-coated PCF for human immunoglobulin G (IgG) detection has been prepared. The end face microscope diagram of the PCF and the fusing splice images of the multimode fiber (MMF) PCF are shown in Figs. 20(a) and 20(b). In order to

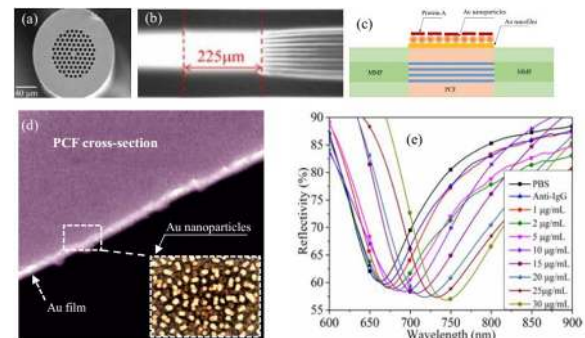


Fig. 20. (a) End face microscope diagram of PCF. (b) Fusing splice image of MMF-PCF. (c) Schematic diagrams of surface functionalization and immune-sensing process. (d) SEM of Au film on the fiber. (e) Optical properties of the sensor in the immobilization and human IgG^[145].

Table 4. Comparisons of Plasmonic PCF Sensors.

Ref.	Fiber Type	Sensing Region	Detection Range	Sensitivity
[145]	MMF-PCF	Protein A/Au NPs/Au film	1-15 $\mu\text{g/mL}$	3915 nm/RIU
[146]	MMF-PCF-MMF	Au/PDMS film	1.33-1.39 RIU	4613.73 nm/RIU
[147]	SMF-MMF-PCF	Collapsed region	$\mu\epsilon_0$ -5000	-2.21 pm/ $\mu\epsilon$
[148]	GO-coated PCF	Collapsed regions	$\mu\epsilon_0$ -1000	3.1 pm/ $\mu\epsilon$
[149]	Ferrofluid-coated PCF	Fiber taper	100-600 Gs	16.04 pm/ $\mu\epsilon$
[150]	V-shaped PCF	Au film	1.333-1.385 RIU	3376 nm/RIU
[151]	Exposed-core PCF	Ag film	1.33-1.37 RIU	1800 nm/RIU
[152]	D-shaped PCF	Au film	1.40-1.42 RIU	7381 nm/RIU
[153]	D-shaped PCF	Au film	1.3388-1.3638 RIU	2336.2 nm/RIU
[154]	Hollow-core PCF	Ag nanoparticles	Not applicable	10^{-10} mol/L
[155]	Suspended-core PCF	Ag core/gold shell	Not applicable	10^{-7} - 10^{-5} mol/L
[156]	Hollow core PCF	Au nanoparticles	Not applicable	200 $\mu\text{g/mL}$
[157]	D-shaped MMF	Au film	1.343-1.373 RIU	3513.3 nm/RIU
[158]	Hollow core PCF	Ag nanoparticles	Not applicable	300 cells/mL

obtain a uniform Au film, a fiber rotating device is adopted to rotate the fiber continuously during the coating process. Figure 20(c) shows the schematic diagram of the PCF sensor with Au film and Au nanoparticle modification. The SEM image of the Au film on the fiber sensor surface is shown in Fig. 20(d). The resonant wavelength variation under different concentrations of human IgG for the protein A-Au nanoparticles-Au-PCF sensor is shown in Fig. 20(e). The detection limit of human IgG based on the protein A-Au nanoparticles-Au-PCF sensor is 37 ng/mL. The RI sensitivity of the sensor reaches 3915 nm/RIU, which is nearly 1.6 times higher than that of the Au-coated PCF sensor without Au nanoparticles. In addition, different PCF structures such as metal-filled PCFs, metal-coated PCFs, and nanoparticles-based plasmonic PCFs have been designed to improve the sensing response, and Table 4 summarizes the main characteristics of these plasmonic PCF devices. It is seen from Table 4 that PCF sensors based on the SPR effect have been successfully used to detect temperature, strain, magnetic field, human IgG, and cell concentrations, exhibiting much better performances. The sensors consist of single PCFs coated with plasmonic nanomaterials and can also be composed of SMF/MMF and PCF.

4. Conclusion and Perspectives

PCF-SPR sensors are receiving increasing attention because of better merits compared to the conventional prism-type SPR configuration, so that extremely high sensitivity can be obtained

based on SPR. There has been tremendous progress in theoretical simulation and experimental fabrication of PCF-SPR sensors. Based on FEM, PCF-SPR sensors with various structures have been designed and evaluated numerically, for instance, side-polished, dual-core cladding with open rings, and dual-beam, liquid-filled cladding coated by plasmonic nanomaterials. These PCF-SPR sensors deliver excellent performance theoretically such as the wide RI detection range of 1.0-1.79, high wavelength sensitivity up to 116,000 nm/RIU, and wide operating wavelength ranges spanning the visible to mid-infrared regime and have enormous potential in bio-sensing, medicine, biology, and trace analysis.

However, not all aspects of PCF-SPR sensors are well understood. Most of the efforts have been devoted to numerical calculation and simulation of the PCF-SPR sensor design. There are a few key barriers that are preventing more widespread implementation. The biggest obstacle is concerned with the fabrication of PCF-SPR sensors, especially deposition of high-quality plasmonic materials on the air hole inner walls inside the PCFs. Theoretical calculation shows that performances of the sensors depend on parameters such as the air hole size, plasmonic material thickness, and fiber core diameters. In addition, although plasmonic materials can be filled in the air hole channels in the PCFs by high-pressure chemical deposition, high-temperature pressure injection, and pressure-assisted splicing techniques, these techniques are quite complex from the manufacturing perspective, and more efforts are needed to develop simple and reliable fabrication techniques for plasmonic materials.

Spurred by advances in micro-fabrication technology, sensitive plasmonic materials can be deposited by advanced surface micro/nano-manufacturing techniques to produce high-performance PCF-SPR sensors. Among the different structures, the D-shaped PCFs have large potential from the viewpoint of fabrication. The D-shaped PCF-SPR sensors possess the advantage of relatively easy side polishing, and plasmonic materials can be fabricated by physical deposition techniques such as RF/DC magnetron sputtering, electron beam evaporation, and chemical synthesis. The sensitive metal layer can be coated adjacent to the core of the PCFs to promote the interactions with the analyte and enhance the sensing performance. In addition, alternative plasmonic materials like graphene, bornene, MoS₂, and other 2D materials with unique physical properties are being explored and expected to improve PCF-SPR sensors in specific applications. The field of PCF-SPR sensing is vibrant, and a better fundamental understanding and continuous technological advances will expedite commercial development.

Acknowledgement

This work was jointly supported by the National Natural Science Foundation of China (No. 51474069), the Local Universities Reformation and Development Personnel Training Supporting Project from Central Authorities (No. 140119001), the Heilongjiang Postdoctoral Foundation (No. LBH-Q20081), and the City University of Hong Kong Strategic Research Grant (SRG) (Nos. 7005105 and 7005265).

References

- W. L. Barnes, A. Dereux, and T. W. Ebbesen, "Surface plasmon subwavelength optics," *Nature* **424**, 824 (2003).
- D. Gong, Y. Yuan, L. Liang, and M. Yang, "Theoretical study on negative permittivity of the material producing sharp surface plasmon resonance dips," *Chin. Opt. Lett.* **17**, 042801 (2019).
- J. Homola, "Surface plasmon resonance sensors for detection of chemical and biological species," *Chem. Rev.* **108**, 462 (2008).
- B. Lee, S. Roh, and J. Park, "Current status of micro- and nano-structured optical fiber sensors," *Opt. Fiber Technol.* **15**, 209 (2009).
- S. Weng, L. Pei, J. Wang, T. Ning, and J. Li, "High sensitivity side-hole fiber magnetic field sensor based on surface plasmon resonance," *Chin. Opt. Lett.* **14**, 110603 (2016).
- J. W. Chung, S. D. Kim, R. Bernhardt, and J. C. Pyun, "Application of SPR biosensor for medical diagnostics of human hepatitis B virus (hHBV)," *Sens. Actuators B Chem.* **111–112**, 416 (2005).
- C. Liu, J. W. Wang, X. Jin, F. M. Wang, L. Yang, J. W. Lv, G. L. Fu, X. L. Li, Q. Liu, T. Sun, and P. K. Chu, "Near-infrared surface plasmon resonance sensor based on photonic crystal fiber with big open rings," *Optik* **207**, 164466 (2020).
- R. C. Jorgenson and S. S. Yee, "A fiber-optic chemical sensor based on surface plasmon resonance," *Sens. Actuators B Chem.* **12**, 213 (1993).
- R. W. Wood, "On a remarkable case of uneven distribution of light in a diffraction grating spectrum," in *Proceedings of the Physical Society of London* (1902), p. 269.
- A. Otto, "Excitation of nonradiative surface plasma waves in silver by the method of frustrated total reflection," *Zeitschrift fur Physik* **216**, 398 (1968).
- E. Kretschmann and H. Raether, "Radiative decay of non-radiative surface plasmons excited by light," *Zeitschrift fur Naturforschung A* **23**, 2135 (1968).
- T. Xue, W. Liang, Y. Li, Y. Sun, Y. Xiang, Y. Zhang, Z. Dai, Y. Duo, L. Wu, K. Qi, B. N. Shivananju, L. Zhang, X. Cui, H. Zhang, and Q. Bao, "Ultrasensitive detection of miRNA with an antimonene-based surface plasmon resonance sensor," *Nat. Commun.* **10**, 28 (2019).
- X. Wang, J. Zhu, Y. Xu, Y. Qi, L. Zhang, H. Yang, and Z. Yi, "A novel plasmonic refractive index sensor based on gold/silicon complementary grating structure," *Chin. Phys. B* **30**, 024207 (2021).
- X. Wang, Y. Wu, X. Wen, J. Zhu, X. Bai, Y. Qi, and H. Yang, "Surface plasmons and SERS application of Au nanodisk array and Au thin film composite structure," *Opt. Quantum Electron.* **52**, 238 (2020).
- E. Klantsataya, P. Jia, H. Ebdorff-Heidepriem, T. M. Monro, and A. François, "Plasmonic fiber optic refractometric sensors: from conventional architectures to recent design trends," *Sensors* **17**, 12 (2017).
- Q. Li, Q. Wang, X. Yang, K. Wang, H. Zhang, and W. Nie, "High sensitivity surface plasmon resonance biosensor for detection of microRNA and small molecule based on graphene oxide-gold nanoparticles composites," *Talanta* **174**, 521 (2017).
- B. D. Gupta, A. M. Shrivastav, and S. P. Usha, "Surface plasmon resonance-based fiber optic sensors utilizing molecular imprinting," *Sensors* **16**, 1381 (2016).
- C. Caucheteur, T. Guo, F. Liu, B. Guan, and J. Albert, "Ultrasensitive plasmonic sensing in air using optical fibre spectral combs," *Nat. Commun.* **7**, 13371 (2016).
- C. Caucheteur, T. Guo, and J. Albert, "Review of plasmonic fiber optic biochemical sensors: improving the limit of detection," *Anal. Bioanal. Chem.* **407**, 3883 (2015).
- J. Lu, T. van Stappen, D. Spasic, F. Delport, S. Vermeire, A. Gils, and J. Lammertyn, "Fiber optic-SPR platform for fast and sensitive infliximab detection in serum of inflammatory bowel disease patients," *Biosens. Bioelectron.* **79**, 173 (2016).
- A. G. Brolo, "Plasmonics for future biosensors," *Nat. Photon.* **6**, 709 (2012).
- C. Liu, G. L. Fu, F. M. Wang, Z. Yi, C. H. Xu, L. Yang, Q. Liu, W. Liu, X. L. Li, H. W. Mu, T. Sun, and P. K. Chu, "Ex-centric core photonic crystal fiber sensor with gold nanowires based on surface plasmon resonance," *Optik* **196**, 163173 (2019).
- Y. Zhang, Z. Yi, X. Wang, P. Chu, W. Yao, Z. Zhou, S. Cheng, Z. Liu, P. Wu, M. Pan, and Y. Yi, "Dual band visible metamaterial absorbers based on four identical ring patches," *Physica E: Low-dimensional Syst. Nanostruct.* **127**, 114526 (2021).
- T. Guo, "Fiber grating assisted surface plasmon resonance for biochemical and electrochemical sensing," *J. Lightwave Technol.* **35**, 3323 (2017).
- X. Wang, H. Deng, and L. Yuan, "Highly sensitive flexible SPR sensor based on side-polishing helical-core fiber: theoretical analysis and experimental demonstration," *Adv. Photon. Res.* **2**, 2000054 (2021).
- J. Ji and L. Yuan, "Transmission enhanced SPR resonance nano-microscope," *Opt. Express* **28**, 22297 (2020).
- Y. Li, H. Ma, L. Gan, Q. Liu, Z. Yan, D. Liu, and Q. Sun, "Immobilized optical fiber microprobe for selective and high sensitive glucose detection," *Sens. Actuators B Chem.* **255**, 3004 (2018).
- Z. Zhang, J. He, B. Du, K. Guo, and Y. Wang, "Highly sensitive gas refractive index sensor based on hollow-core photonic bandgap fiber," *Opt. Express* **27**, 29649 (2019).
- Z. Bai, M. Li, Y. Wang, J. Tang, Z. Zhang, S. Liu, C. Fu, Y. Zhang, J. He, Y. Wang, and C. Liao, "Orbital angular momentum generator based on hollow-core photonic bandgap fiber grating," *Appl. Phys. Express* **12**, 072004 (2019).
- C. Fu, S. Liu, Y. Wang, Z. Bai, J. He, C. Liao, Y. Zhang, F. Zhang, B. Yu, S. Gao, Z. Li, and Y. Wang, "High-order orbital angular momentum mode generator based on twisted photonic crystal fiber," *Opt. Lett.* **43**, 1786 (2018).
- P. Russell, "Applied physics: photonic crystal fibers," *Science* **299**, 358 (2003).
- J. Han, E. Liu, and J. Liu, "Circular gradient-diameter photonic crystal fiber with large mode area and low bending loss," *J. Opt. Soc. Am. A* **36**, 533 (2019).
- Z. Huo, E. Liu, and J. Liu, "Hollow-core photonic quasicrystal fiber with high birefringence and ultra-low nonlinearity," *Chin. Opt. Lett.* **18**, 030603 (2020).
- S. A. S. Hashemi and M. Noorim, "Dispersion tailoring of photonic crystal fibers for flat-top, coherent, and broadband supercontinuum generation," *Phys. Scrip.* **95**, 075501 (2020).
- T. V. Andersen, K. M. Hilligsøe, C. K. Nielsen, J. Thøgersen, K. P. Hansen, S. R. Keiding, and J. J. Larsen, "Continuous-wave wavelength conversion in a photonic crystal fiber with two zero-dispersion wavelengths: erratum," *Opt. Express* **13**, 3581 (2005).

36. J. M. Dudley, G. Genty, and S. Coen, "Supercontinuum generation in photonic crystal fiber," *Rev. Mod. Phys.* **78**, 1135 (2006).
37. A. Hassani and M. Skorobogatiy, "Design of the microstructured optical fiber-based surface plasmon resonance sensors with enhanced microfluidics," *Opt. Express* **14**, 11616 (2006).
38. J. Luo, S. Chen, H. Qu, Z. Su, L. Li, and F. Tian, "Highly birefringent single-mode suspended-core fiber in terahertz regime," *J. Lightwave Technol.* **36**, 3242 (2018).
39. J. Wang, C. Liu, F. Wang, W. Su, L. Yang, J. Lv, G. Fu, X. Li, Q. Liu, T. Sun, and P. K. Chu, "Surface plasmon resonance sensor based on coupling effects of dual photonic crystal fibers for low refractive indexes detection," *Results Phys.* **18**, 103240 (2020).
40. X. Yang, Y. Lu, M. Wang, and J. Yao, "An exposed-core grapefruit fibers based surface plasmon resonance sensor," *Sensors* **15**, 17106 (2015).
41. C. Liu, J. W. Wang, F. M. Wang, W. Q. Su, L. Yang, J. W. Lv, G. L. Fu, X. L. Li, Q. Liu, T. Sun, and P. K. Chu, "Surface plasmon resonance (SPR) infrared sensor based on D-shape photonic crystal fibers with ITO coatings," *Opt. Commun.* **464**, 125496 (2020).
42. A. A. Rifat, G. A. Mahdiraji, D. M. Chow, G. S. Yu, R. Ahmed, and F. R. M. Adikan, "Photonic crystal fiber-based surface plasmon resonance sensor with selective analyte channels and graphene-silver deposited core," *Sensors* **15**, 11499 (2015).
43. G. An, S. Li, W. Qin, W. Zhang, Z. Fan, and Y. Bao, "High-sensitivity refractive index sensor based on D-shaped photonic crystal fiber with rectangular lattice and nanoscale gold film," *Plasmonics* **9**, 1355 (2014).
44. Y. Zhao, Z. Deng, and J. Li, "Photonic crystal fiber based surface plasmon resonance chemical sensors," *Sens. Actuators B Chem.* **202**, 557 (2014).
45. D. J. J. Hu and H. P. Ho, "Recent advances in plasmonic photonic crystal fibers: design, fabrication and applications," *Adv. Opt. Photon.* **9**, 257 (2017).
46. B. D. Gupta and R. K. Verma, "Surface plasmon resonance-based fiber optic sensors: principle, probe designs, and some applications," *J. Sens.* **2009**, 979761 (2009).
47. A. Guerreiro, D. F. Santos, and J. M. Baptista, "New trends in the simulation of nanosplasmic optical D-type fiber sensors," *Sensors* **19**, 1772 (2019).
48. A. K. Sharma, A. K. Pandey, and B. Kaur, "A review of advancements (2007–2017) in plasmonics-based optical fiber sensors," *Opt. Fiber Technol.* **43**, 20 (2018).
49. H. Raether, *Surface Plasmons on Smooth and Rough Surfaces and on Gratings* (Springer, 1988).
50. N. Luan, R. Wang, W. Lv, and J. Yao, "Surface plasmon resonance sensor based on D-shaped microstructured optical fiber with hollow core," *Opt. Express* **23**, 8576 (2015).
51. D. Gao, C. Y. Guan, Y. W. Wen, X. Zhong, and L. B. Yuan, "Multi-hole fiber based surface plasmon resonance sensor operated at near-infrared wavelengths," *Opt. Commun.* **313**, 94 (2014).
52. A. Hassani and M. Skorobogatiy, "Design criteria for microstructured-optical-fiber based surface-plasmon-resonance sensors," *J. Opt. Soc. Am. B* **24**, 1423 (2007).
53. F. Hao and P. Nordlander, "Efficient dielectric function for FDTD simulation of the optical properties of silver and gold nanoparticles," *Chem. Phys. Lett.* **446**, 115 (2007).
54. A. Vial and T. Laroche, "Comparison of gold and silver dispersion laws suitable for FDTD simulations," *Appl. Phys. B* **93**, 139 (2008).
55. W. Qin, S. Li, J. Xue, X. Xin, and L. Zhang, "Numerical analysis of a photonic crystal fiber based on two polarized modes for biosensing applications," *Chin. Phys. B* **22**, 074213 (2013).
56. A. K. Mishra, S. K. Mishra, and B. D. Gupta, "SPR based fiber optic sensor for refractive index sensing with enhanced detection accuracy and figure of merit in visible region," *Opt. Commun.* **344**, 86 (2015).
57. A. Hassani and M. Skorobogatiy, "Photonic crystal fiber-based plasmonic sensors for the detection of biolayer thickness," *J. Opt. Soc. Am. B* **26**, 1550 (2009).
58. F. Wang, C. Liu, Z. Sun, T. Sun, B. Liu, and P. K. Chu, "A highly sensitive SPR sensors based on two parallel PCFs for low refractive index detection," *IEEE Photon. J.* **10**, 7104010 (2018).
59. T. Bellunato, M. Calvi, C. Matteuzzi, M. Musy, D. L. Perego, and B. Storaci, "Refractive index of silica aerogel: uniformity and dispersion law," *Nucl. Instrum. Methods Phys. Res. A* **595**, 183 (2008).
60. X. Chen, L. Xia, and C. Li, "Surface plasmon resonance sensor based on a novel D-shaped photonic crystal fiber for low refractive index detection," *IEEE Photon. J.* **10**, 6800709 (2018).
61. A. L. Leal, M. C. Estevez, S. O. M. Chapa, and L. M. Lechug, "Design of a surface plasmon resonance immunoassay for therapeutic drug monitoring of amikacin," *Talanta* **141**, 253 (2015).
62. C. Liu, L. Yang, Q. Liu, F. Wang, Z. Sun, T. Sun, H. Mu, and P. K. Chu, "Analysis of a surface plasmon resonance probe based on photonic crystal fibers for low refractive index detection," *Plasmonics* **13**, 779 (2018).
63. C. Liu, L. Yang, X. Lu, Q. Liu, F. Wang, J. Lv, T. Sun, H. Mu, and P. K. Chu, "Mid-infrared surface plasmon resonance sensor based on photonic crystal fibers," *Opt. Express* **25**, 14227 (2017).
64. E. Haque, M. A. Hossain, T. Pham, Y. Namihira, N. H. Hai, and F. Ahmed, "Surface plasmonic resonance sensor for wider range of low refractive index detection," in *The 26th International Conference on Telecommunications* (2019).
65. W. Zeng, Q. Wang, and L. Xu, "Plasmonic refractive index sensor based on D-shaped photonic crystal fiber for wider range of refractive index detection," *Optik* **223**, 165463 (2020).
66. E. Haque, M. A. Hossain, Y. Namihira, and F. Ahmed, "Microchannel-based plasmonic refractive index sensor for low refractive index detection," *Appl. Opt.* **58**, 1547 (2019).
67. B. Liu, Y. Jiang, X. Zhu, X. Tang, and Y. Shi, "Hollow fiber surface plasmon resonance sensor for the detection of liquid with high refractive index," *Opt. Express* **21**, 32349 (2013).
68. S. Chu, K. Nakkeeran, A. M. Abobaker, S. S. Aphale, P. R. Babu, and K. Senthilnathan, "Design and analysis of surface-plasmon-resonance-based photonic quasi-crystal fiber biosensor for high-refractive-index liquid analytes," *IEEE J. Sel. Top. Quantum Electron.* **25**, 6900309 (2019).
69. S. Chu, K. Nakkeeran, A. M. Abobaker, S. S. Aphale, S. Sivabalan, P. R. Babu, and K. Senthilnathan, "A surface plasmon resonance bio-sensor based on dual core D-shaped photonic crystal fibre embedded with silver nanowires for multi-sensing," *IEEE Sens. J.* **21**, 76 (2020).
70. K. Tong, F. C. Wang, M. T. Wang, P. Dang, Y. X. Wang, and J. R. Sun, "D-Shaped photonic crystal fiber biosensor based on silver-graphene," *Optik* **168**, 467 (2018).
71. F. D. Apuzzo, A. R. Piacenti, F. Giorgianni, M. Autore, M. C. Guidi, A. Marcellini, U. Schade, Y. Ito, M. Chen, and S. Lupi, "Terahertz and mid-infrared plasmons in three-dimensional nanoporous graphene," *Nat. Commun.* **8**, 14885 (2017).
72. A. A. Rifat, R. Ahmed, G. A. Mahdiraji, and F. R. M. Adikan, "Highly sensitive D-shaped photonic crystal fiber-based plasmonic biosensor in visible to near-IR," *IEEE Sens. J.* **17**, 2776 (2017).
73. M. De and V. K. Singh, "Analysis of a highly sensitive flat fiber plasmonic refractive index sensor," *Appl. Opt.* **59**, 380 (2020).
74. M. S. A. Gandhi, K. Senthilnathan, P. R. Babu, and Q. Li, "Highly sensitive localized surface plasmon polariton based D-type twin-hole photonic crystal fiber microbiosensor: enhanced scheme for SERS reinforcement," *Sensors* **20**, 5248 (2020).
75. G. An, S. Li, X. Yan, X. Zhang, Z. Yuan, H. Wang, Y. Zhang, X. Hao, Y. Shao, and Z. Han, "Extra-broad photonic crystal fiber refractive index sensor based on surface plasmon resonance," *Plasmonics* **12**, 465 (2017).
76. E. Haque, M. A. Hossain, F. Ahmed, and Y. Namihira, "Surface plasmon resonance sensor based on modified D-shaped photonic crystal fiber for wider range of refractive index detection," *IEEE Sens. J.* **18**, 8287 (2018).
77. G. An, X. Hao, S. Li, X. Yan, and X. Zhang, "D-shaped photonic crystal fiber refractive index sensor based on surface plasmon resonance," *Appl. Opt.* **56**, 6988 (2017).
78. J. N. D. R. Jha, "On the performance of graphene-based D shaped photonic crystal fibre biosensor using surface plasmon resonance," *Plasmonics* **10**, 1123 (2015).
79. U. Lu, Y. Li, Y. Han, Y. Liu, and J. Gao, "D-shaped photonic crystal fiber plasmonic refractive index sensor based on gold grating," *Appl. Opt.* **57**, 5268 (2018).
80. G. An, S. Li, H. Wang, and X. Zhang, "Metal oxide-graphene-based quasi-D-shaped optical fiber plasmonic biosensor," *IEEE Photon. J.* **9**, 6803909 (2017).
81. J. Liu, H. Liang, B. Liu, X. He, and Z.-P. Chen, "Abnormal sensing properties of surface plasmon resonance sensor based on photonic crystal fibers," *Opt. Fiber Technol.* **48**, 248 (2019).

82. F. Haider, R. A. Aoni, R. Ahmed, and A. E. Miroshnichenko, "Highly amplitude-sensitive photonic crystal-fiber-based plasmonic sensor," *J. Opt. Soc. Am. B* **35**, 2816 (2018).
83. Q. Liu, J. Sun, Y. Sun, W. Liu, F. Wang, L. Yang, C. Liu, Q. Liu, Q. Li, Z. Ren, T. Sun, and P. K. Chu, "Surface plasmon resonance sensor based on eccentric core photonic quasi-crystal fiber with indium tin oxide," *Appl. Opt.* **58**, 6848 (2019).
84. A. K. Paul, A. K. Sarkar, A. B. S. Rahman, and A. Khaleque, "Twin core photonic crystal fiber plasmonic refractive index sensor," *IEEE Sens. J.* **18**, 5761 (2018).
85. D. Ristau and H. Ehlers, *Thin Film Optical Coating in Springer Handbook of Lasers and Optics* (Springer, 2012).
86. R. Otupiri, E. K. Akowuah, and S. Haxha, "Multi-channel SPR biosensor based on PCF for multi-analyte sensing applications," *Opt. Express* **23**, 15716 (2015).
87. D. Li, W. Zhang, H. Liu, J. Hu, and G. Zhou, "High sensitivity refractive index sensor based on multicoating photonic crystal fiber with surface plasmon resonance at near-infrared wavelength," *IEEE Photon. J.* **9**, 6801608 (2017).
88. C. Liu, W. Su, F. Wang, X. Li, Q. Liu, H. Mu, T. Sun, P. K. Chu, and B. Liu, "Birefringent PCF-based SPR sensor for a broad range of low refractive index detection," *IEEE Photon. Tech. Lett.* **30**, 1471 (2018).
89. C. Liu, W. Su, Q. Liu, X. Lu, F. Wang, T. Sun, and P. K. Chu, "Symmetrical dual D-shape photonic crystal fibers for surface plasmon resonance sensing," *Opt. Express* **26**, 9039 (2018).
90. Z. Yang, L. Xia, C. Li, X. Chen, and D. Liu, "A surface plasmon resonance sensor based on concave-shaped photonic crystal fiber for low refractive index detection," *Opt. Commun.* **430**, 195 (2019).
91. G. Wang, Y. Lu, L. Duan, and J. Yao, "A refractive index sensor based on PCF with ultra-wide detection range," *IEEE J. Sel. Top. Quantum Electron.* **27**, 5600108 (2020).
92. M. R. Islam, M. M. I. Khan, F. Mehjabin, J. A. Chowdhury, and M. Islam, "Design of a fabrication friendly and highly sensitive surface plasmon resonance-based photonic crystal fiber biosensor," *Results Phys.* **19**, 103501 (2020).
93. A. A. Rifat, G. A. Mahdiraji, R. Ahmed, D. M. Chow, Y. M. Sua, Y. G. Shee, and F. R. M. Adikan, "Copper-graphene based photonic crystal fiber plasmonic biosensor," *IEEE Photon. J.* **8**, 4800408 (2016).
94. A. A. Rifat, M. R. Hasan, R. Ahmed, and H. Butt, "Photonic crystal fiber-based plasmonic biosensor with external sensing approach," *J. Nanophoton.* **12**, 012503 (2017).
95. A. A. Rifat, F. Haider, R. Ahmed, G. A. Mahdiraji, F. R. M. Adikan, and A. E. Miroshnichenko, "Highly sensitive selectively coated photonic crystal fiber-based plasmonic sensor," *Opt. Lett.* **43**, 891 (2018).
96. X. C. Yang, Y. Lu, M. T. Wang, and J. Q. Yao, "SPR sensor based on exposed-core grapefruit fiber with bimetallic structure," *IEEE Photon. Tech. Lett.* **28**, 649 (2016).
97. P. B. Bing, S. C. Huang, J. L. Sui, H. Wang, and Z. Y. Wang, "Analysis and improvement of a dual-core photonic crystal fiber sensor," *Sensors* **18**, 2051 (2018).
98. M. R. Momota and M. R. Hasan, "Hollow-core silver coated photonic crystal fiber plasmonic sensor," *Opt. Mater.* **76**, 287 (2018).
99. Q. Liu, J. Sun, Y. Sun, W. Liu, J. Lv, C. Liu, X. Li, Z. Ren, F. Wang, W. Lu, Y. Jiang, T. Sun, and P. K. Chu, "High-sensitivity SPR sensor based on the eightfold eccentric core PQF with locally coated indium tin oxide," *Appl. Opt.* **59**, 6484 (2020).
100. M. De, C. Markides, V. K. Singh, C. Themistos, and B. M. A. Rahman, "Analysis of a single solid core flat fiber plasmonic refractive index sensor," *Plasmonics* **15**, 1429 (2020).
101. Y. Lu, X. Yang, M. Wang, and J. Yao, "Surface plasmon resonance sensor based on hollow-core PCFs filled with silver nanowires," *Electron. Lett.* **51**, 1675 (2015).
102. M. A. Mahfuz, M. A. Hossain, E. Haque, N. H. Hai, Y. Namihira, and F. Ahmed, "Dual-core photonic crystal fiber-based plasmonic RI sensor in the visible to near-IR operating band," *IEEE Sens. J.* **20**, 7692 (2020).
103. M. Liu, X. Yang, B. Zhao, J. Hou, and P. Shum, "Square array photonic crystal fiber-based surface plasmon resonance refractive index sensor," *Mod. Phys. Lett. B* **31**, 1750352 (2017).
104. W. Liu, F. Wang, C. Liu, L. Yang, Q. Liu, W. Su, J. Lv, S. An, X. Li, T. Sun, and P. K. Chu, "A hollow dual-core PCF-SPR sensor with gold layers on the inner and outer surfaces of the thin cladding," *Results Opt.* **1**, 100004 (2020).
105. J. N. Dash and R. Jha, "Highly sensitive side-polished birefringent PCF-based SPR sensor in near IR," *Plasmonics* **11**, 1505 (2016).
106. N. Chen, M. Chang, X. Zhang, J. Zhou, X. Lu, and S. Zhuang, "Highly sensitive plasmonic sensor based on a dual-side polished photonic crystal fiber for component content sensing applications," *Nanomaterials* **9**, 1587 (2019).
107. H. Han, D. Hou, N. Luan, Z. Bai, L. Song, J. Liu, and Y. Hu, "Surface plasmon resonance sensor based on dual-side polished microstructured optical fiber with dual-core," *Sensors* **20**, 3911 (2020).
108. T. Li, L. Zhu, X. Yang, X. Lou, and L. Yu, "A refractive index sensor based on H-shaped photonic crystal fibers coated with Ag-graphene layers," *Sensors* **20**, 741 (2020).
109. O. Salihoglu, S. Balci, and C. Kocabas, "Plasmon-polaritons on graphene-metal surface and their use in biosensors," *Appl. Phys. Lett.* **100**, 213110 (2012).
110. J. S. Bunch, A. M. V. Zanda, S. S. Verbridge, I. W. Frank, D. M. Tanenbaum, J. M. Parpia, H. G. Craighead, and P. L. McEuen, "Electromechanical resonators from graphene sheets," *Science* **315**, 490 (2007).
111. H. Han, D. Hou, L. Zhao, N. Luan, L. Song, Z. Liu, Y. Lian, J. Liu, and Y. Hu, "A large detection-range plasmonic sensor based on an H-shaped photonic crystal fiber," *Sensors* **20**, 1009 (2020).
112. C. Li, B. Yan, and J. Liu, "Refractive index sensing characteristics in a D-shaped photonic quasi-crystal fiber sensor based on surface plasmon resonance," *J. Opt. Soc. Am. A* **36**, 1663 (2019).
113. A. K. Paul, M. S. Habib, N. H. Hai, and S. M. A. Razzak, "An air-core photonic crystal fiber based plasmonic sensor for high refractive index sensing," *Opt. Commun.* **464**, 125556 (2020).
114. A. K. Paul, "Design and analysis of photonic crystal fiber plasmonic refractive index sensor for condition monitoring of transformer oil," *OSA Continuum* **3**, 2253 (2020).
115. H. Abdullah, K. Ahmed, and S. A. Mitu, "Ultrahigh sensitivity refractive index biosensor based on gold coated nano-film photonic crystal fiber," *Results Phys.* **17**, 103151 (2020).
116. S. Singh and Y. K. Prajapati, "TiO₂/gold-graphene hybrid solid core SPR based PCF RI sensor for sensitivity enhancement," *Optik* **224**, 165525 (2020).
117. P. Bing, J. Sui, G. Wu, X. Guo, Z. Li, L. Tan, and J. Yao, "Analysis of dual-channel simultaneous detection of photonic crystal fiber sensors," *Plasmonics* **15**, 1071 (2020).
118. F. Haider, R. A. Aoni, R. Ahmed, G. A. Mahdiraji, M. F. Azman, and F. R. M. Adikan, "Mode-multiplex plasmonic sensor for multi-analyte detection," *Opt. Lett.* **45**, 3945 (2020).
119. X. Meng, J. Li, Y. Guo, S. Li, Y. Wang, W. Bi, and H. Lu, "An optical-fiber sensor with double loss peaks based on surface plasmon resonance," *Optik* **216**, 164938 (2020).
120. S. Hossain, M. R. I. Sheikh, T. Ahmed, and I. Mahmud, "Design of a surface plasmon resonance based gold coated photonic crystal fiber biosensor," in *The 4th International Conference on Electrical Information and Communication Technology* (2019).
121. T. Wu, Y. Shao, Y. Wang, S. Cao, W. Cao, F. Zhang, C. Liao, J. He, Y. Huang, M. Hou, and Y. Wang, "Surface plasmon resonance biosensor based on gold-coated side-polished hexagonal structure photonic crystal fiber," *Opt. Express* **25**, 20313 (2017).
122. M. A. Mahfuz, M. A. Hossain, E. Haque, N. H. Hai, Y. Namihira, and F. Ahmed, "A bimetallic-coated, low propagation loss, photonic crystal fiber based plasmonic refractive index sensor," *Sensors* **19**, 3794 (2019).
123. G. Melwin and K. Senthilnathan, "High sensitive D-shaped photonic crystal fiber sensor with V-groove analyte channel," *Optik* **213**, 164779 (2020).
124. E. Haque, S. Mahmuda, M. A. Hossain, N. H. Hai, Y. Namihira, and F. Ahmed, "Highly sensitive dual-core PCF based plasmonic refractive index sensor for low refractive index detection," *IEEE Photon. J.* **11**, 7905309 (2019).
125. Z. Liu and H. Tam, "Fabrication and sensing applications of special microstructured optical fibers," in *Selected Topics on Optical Fiber Technologies and Applications* (INTECH, 2018), Chap. 1.
126. P. J. A. Sazio, A. Amezcua-Correa, C. E. Finlayson, J. R. Hayes, T. J. Scheidemantel, N. F. Baril, B. R. Jackson, D. J. Won, F. Zhang, E. R. Margine, V. Gopalan, V. H. Crespi, and J. V. Badding,

- "Microstructured optical fibers as high-pressure microfluidic reactors," *Science* **311**, 1583 (2006).
127. A. Csaki, F. Jahn, I. Latka, T. Henkel, D. Malsch, T. Schneider, K. Schröder, K. Schuster, A. Schwuchow, R. Spittel, D. Zopf, and W. Fritzsche, "Nanoparticle layer deposition for plasmonic tuning of microstructured optical fibers," *Small* **6**, 2584 (2010).
 128. L. Jiang, C. Yuan, Z. Li, J. Su, Z. Yi, W. Yao, P. Wu, Z. Liu, S. Cheng, and M. Pan, "Multi-band and high-sensitivity perfect absorber based on monolayer graphene metamaterial," *Diam. Relat. Mater.* **111**, 108227 (2021).
 129. Z. Yi, J. Li, J. Lin, F. Qin, X. Chen, W. Yao, Z. Liu, S. Cheng, P. Wu, and H. Li, "Broadband polarization-insensitive and wide-angle solar energy absorber based on tungsten ring-disc array," *Nanoscale* **12**, 23077 (2020).
 130. P. Chu, J. Chen, Z. Xiong, and Z. Yi, "Controllable frequency conversion in the coupled time-modulated cavities with phase delay," *Opt. Commun.* **476**, 126338 (2020).
 131. X. Zhang, X. Zhu, and Y. Shi, "Fiber optic surface plasmon resonance sensor based on silver-coated large-core suspended-core fiber," *Opt. Lett.* **44**, 4550 (2019).
 132. B. Doherty, A. Csaki, M. Thiele, M. Zeisberger, A. Schwuchow, J. Kobelke, W. Fritzsche, and M. A. Schmidt, "Nanoparticle functionalised small-core suspended-core fibre - a novel platform for efficient sensing," *Biomed. Opt. Express* **8**, 790 (2017).
 133. K. Schroder, A. Csaki, A. Schwuchow, F. Jahn, K. Strelau, I. Latka, T. Henkel, D. Malsch, K. Schuster, K. Weber, T. Schneider, R. Moller, and W. Fritzsche, "Functionalization of microstructured optical fibers by internal nanoparticle mono-layers for plasmonic biosensor applications," *IEEE Sens. J.* **12**, 218 (2012).
 134. H. W. Lee, M. A. Schmidt, R. F. Russell, N. Y. Joly, H. K. Tyagi, P. Uebel, and P. S. J. Russell, "Pressure-assisted melt-filling and optical characterization of Au nano-wires in microstructured fibers," *Opt. Express* **19**, 12180 (2011).
 135. M. J. Weber, *Handbook of Optical Materials* (CRC Press, 2002).
 136. N. Da, L. Wondraczek, M. A. Schmidt, N. Granzow, and P. S. J. Russell, "High index-contrast all-solid photonic crystal fibers by pressure-assisted melt infiltration of silica matrices," *J. Non-Crystal Solids* **356**, 1829 (2010).
 137. H. W. Lee, M. A. Schmidt, H. K. Tyagi, L. P. Sempere, and P. S. J. Russell, "Polarization-dependent coupling to plasmon modes on submicron gold wire in photonic crystal fiber," *Appl. Phys. Lett.* **93**, 111102 (2008).
 138. M. Schmidt, L. Prill Sempere, H. Tyagi, C. Poulton, and P. Russell, "Waveguiding and plasmon resonances in two-dimensional photonic lattices of gold and silver nanowires," *Phys. Rev. B* **77**, 033417 (2008).
 139. M. A. Schmidt, N. Granzow, N. Da, M. Y. Peng, L. Wondraczek, and P. S. J. Russell, "All-solid bandgap guiding in tellurite-filled silica photonic crystal fibers," *Opt. Lett.* **34**, 1946 (2009).
 140. H. K. Tyagi, M. A. Schmidt, L. Prill Sempere, and P. S. Russell, "Optical properties of photonic crystal fiber with integral micron-sized Ge wire," *Opt. Express* **16**, 17227 (2008).
 141. A. Tuniz, B. T. Kuhlmeier, R. Lwin, A. Wang, J. Anthony, R. Leonhardt, and S. C. Fleming, "Drawn metamaterials with plasmonic response at terahertz frequencies," *Appl. Phys. Lett.* **96**, 191101 (2010).
 142. C. Markos, I. Kubat, and O. Bang, "Hybrid polymer photonic crystal fiber with integrated chalcogenide glass nanofilms," *Sci. Rep.* **4**, 6057 (2014).
 143. B. Li, T. Cheng, J. Chen, and X. Yan, "Graphene-enhanced surface plasmon resonance liquid refractive index sensor based on photonic crystal fiber," *Sensors* **19**, 3666 (2019).
 144. V. Portosi, D. Laneve, M. C. Falconi, and F. Prudenzano, "Advances on photonic crystal fiber sensors and application," *Sensors* **19**, 1892 (2019).
 145. B. Wang and Q. Wang, "Sensitivity-enhanced optical fiber biosensor based on coupling effect between SPR and LSPR," *IEEE Sens. J.* **18**, 8303 (2018).
 146. Y. Wang, Q. Huang, W. Zhu, M. Yang, and E. Lewis, "Novel optical fiber SPR temperature sensor based on MMF-PCF-MMF structure and gold-PDMF film," *Opt. Express* **26**, 1910 (2018).
 147. X. Dong, H. Du, X. Sun, Z. Luo, and J. Duan, "A novel strain sensor with large measurement range based on all fiber Mach-Zehnder interferometer," *Sensors*, **18**, 1549 (2018).
 148. J. N. Dash, N. Negi, and R. Jha, "Graphene oxide coated PCF interferometer for enhanced strain sensitivity," *J. Lightwave Technol.* **35**, 5385 (2017).
 149. Y. Zhao, D. Wu, and R. Q. Lv, "Magnetic field sensor based on photonic crystal fiber taper coated with ferrofluid," *IEEE Photon. Tech. Lett.* **27**, 26 (2015).
 150. L. Liu, Z. Liu, Y. Zhang, and S. Liu, "V-shaped micro-structure optical fiber surface plasmon resonance sensor for the simultaneous measurement of the refractive index and temperature," *Opt. Lett.* **44**, 5093 (2019).
 151. E. Klantsataya, A. Franois, H. E. Heidepriem, P. Hoffmann, and T. M. Monro, "Surface plasmon scattering in exposed core optical fiber for enhanced resolution refractive index sensing," *Sensors*, **15**, 25090 (2015).
 152. Q. Xie, Y. Chen, X. Li, Z. Yin, L. Wang, Y. Geng, and X. Hong, "Characteristics of D-shaped photonic crystal fiber surface plasmon resonance sensors with different side-polished lengths," *Appl. Opt.* **56**, 11550 (2017).
 153. Y. Chen, Q. Xie, X. Li, H. Zhou, X. Hong, and Y. Geng, "Experimental realization of D-shaped photonic crystal fiber SPR sensor," *J. Phys. D: Appl. Phys.* **50**, 025101 (2017).
 154. X. C. Shi, D. Wheeler, R. Newhouse, B. Chen, J. Z. Zhang, and C. Gu, "High-sensitivity molecular sensing using hollow-core photonic crystal fiber and surface-enhanced Raman scattering," *J. Opt. Soc. Am. A* **27**, 308 (2010).
 155. P. Pinkhasova, H. Chen, J. Kanka, P. Mergo, and H. Du, "Nanotag-enabled photonic crystal fiber as quantitative surface-enhanced Raman scattering optofluidic platform," *Appl. Phys. Lett.* **106**, 071106 (2015).
 156. U. S. Dinis, G. Balasundaram, Y. T. Chang, and M. Olivo, "Sensitive multiplex detection of serological liver cancer biomarkers using SERS-active photonic crystal fiber probe," *J. Biophotonics* **7**, 956 (2015).
 157. M. Chen, T. Lang, B. Cao, Y. Yu, and C. Shen, "D-type optical fiber immunoglobulin G sensor based on surface plasmon resonance," *Opt. Laser Technol.* **131**, 106445 (2020).
 158. A. Khetani, A. Momenpour, E. Alarcon, and H. Anis, "Hollow core photonic crystal fiber for monitoring leukemia cells using surface enhanced Raman scattering (SERS)," *Biomed. Opt. Express* **6**, 4599 (2015).